Computers and Geotechnics 174 (2024) 106560

Contents lists available at ScienceDirect

Computers and Geotechnics

journal homepage: www.elsevier.com/locate/compgeo

Research paper

Investigation of strain-sensitive properties of porous media through micro-CT imaging and numerical modelling

Shan Zhong, Xiangyun Ge, Hywel R. Thomas *, Chenfeng Li

Zienkiewicz Institute for Modelling, Data and AI, Swansea University, Swansea, United Kingdom

ARTICLE INFO

Keywords:
Rocks and porous media
In-situ property prediction
Image-based simulation
Discrete Element Method
Stress and strain
Deformation
Contact and fracture

ABSTRACT

Strain-sensitive characteristics of porous media are studied through micro-CT imaging and numerical simulations. First, high-fidelity Discrete Element Method (DEM) models are constructed for practical porous media based on micro-CT images. These DEM models prioritize the overall system morphology over individual grain/particle shapes, ensuring robustness and flexibility controlled by easily adjustable algorithm parameters. Subsequently, we validate the accuracy of our proposed DEM models by comparing them with the Finite Element Method (FEM), achieving consistent agreement across all test cases. Finally, the CT-image based DEM approach is employed to investigate strain-sensitive properties of porous media, such as permeability, porosity, tortuosity, specific surface area, and fractal dimension. With a primary focus on transport and morphology properties, our approach is versatile and applicable to exploring various other properties of porous media. This study introduces a generic methodology for examining practical porous media under in-situ conditions, providing valuable insights into their response to stress and deformation.

1. Introduction

Porous materials are frequently encountered in various substances such as rocks, soil, composites, biological tissues, and metal foams. The deformation of porous materials under stress significantly impacts their properties, notably affecting fluid flow characteristics such as porosity, pore-scale morphology, and permeability. There have been extensive studies investigating the influence of stress on the fluid flow properties of porous media (Gao et al., 2020; Yin et al., 2015; Li et al., 2016). While compression experiments are commonly used to study the macroscopic mechanical properties of porous materials, they offer limited insights into the underlying microscopic processes. Furthermore, these experiments often lead to sample destruction, rendering them unsuitable for reuse in further testing. As a promising alternative, numerical simulations, particularly the Finite Element Method (FEM) and the Discrete Element Method (DEM), have been increasingly adopted to study the properties of porous media under stress and deformation.

1.1. The finite element approach

The FEM is a widely used numerical approach for simulating the deformation of porous materials. Given the complexity of porous media, various averaging and simplification techniques have been developed to study their macro-mechanical behaviour. Gans and Woodmansee (1992) introduced a novel cubic cell model containing different numbers of cubic pores to represent porous materials. Ghosh et al. (2001) employed the Voronoi cell finite element model to investigate macroscopic damage in 2D porous materials. Meanwhile, Roberts and Garboczi (2000) modelled porous media with a sphere packing model, and evaluated the change of Young's modulus concerning porosity. In this model, the overlapping spheres represent either the pore or solid phase. However, these techniques primarily focus on macro-mechanics, overlooking the deformation of microscopic structures. The distribution and shape of pores in these models are typically generated using probabilistic and statistical methods.

With the advancement of micro-CT technology, simulations of porous materials can now be based on real shapes derived from digital samples. Micro-CT-based finite element modelling has become prevalent for investigating the deformation behaviour of porous materials at the microscopic level. Several different methods have been developed to generate finite element models from micro-CT images.

The first approach involves substituting each voxel with a cubic element. van Rietbergen et al. (1995) transformed the rectangular voxels in digital images of trabecular bone into equally sized eight-node brick elements. Similarly, Arns et al. (2002) investigated the linear elastic properties of sandstone from micro-CT images by treating each voxel as a trilinear finite element. However, this method is constrained

---

* Corresponding author.
E-mail address: h.r.thomas@swansea.ac.uk (H.R. Thomas).

https://doi.org/10.1016/j.compgeo.2024.106560

by computing power, and the computational cost increases dramatically when high-resolution images are used.

The second approach entails creating a simplified geometric model based on the micro-structural knowledge derived from CT images. Cortés et al. (2019) developed a new method to construct a truss model for open-cell porous materials using graph theory. Iio et al. (2016) employed a regularly arranged Kelvin cellular model to represent hollow-strut cellular materials, such as metal foams. Hössinger-Kalteis et al. (2021) reviewed different methods for creating ideal or simplified models of cellular porous materials. For granular porous materials, the random sphere packing method, which represents the solid phase with spheres, is commonly adopted to build ideal or simplified models. This approach offers a more effective way to explore the mechanical properties of porous materials. However, the extent to which these simplified models accurately represent real structures remains uncertain, and the inherently irregular structure of real porous materials often emerges as a weakness.

The third approach works by generating a surface mesh of the pore/solid phase on the basis of the micro-CT image, from which a volume mesh can be constructed. An example is presented in Chai et al. (2021), where the binary 3D image of porous titanium was first converted into a surface mesh with triangular elements and after refinement and smoothing, this surface mesh was transformed into a volume mesh using linear tetrahedron elements. In this work, the resulting tetrahedron mesh model was utilized to simulate the uniaxial compression of porous titanium. Other researchers have also adopted a similar framework to study the mechanical properties of porous materials (Doroszko and Seweryn, 2020; Samaei and Chaudhuri, 2021). The generating of surface mesh usually require complex and time costly algorithms, especially for porous media with irregular shape and relatively small sharp corners.

Besides these three popular approaches, other methods have been developed to build FEM models for complex microstructure geometries. For example, Stamati et al. (2019) used a non-adapted mesh method (Moës et al., 2003). In this approach, an FE mesh is first generated independent from morphology features, after which each node is assigned a phase based on the CT-image. The elements whose nodes belong to two different phases are treated as interface, which is processed by a kinematics enhancement (Roubin et al., 2015). This method avoids the surface detection and generation processes, which usually require complex and time costly algorithms.

The FEM is an effective tool for studying the deformation of porous materials, but it inherently struggles with contact problems. This issue is particularly pertinent in granular porous media, such as sandstone and concrete, where deformation is often accompanied by self-contact issues at the surfaces of microscopic pores. To address this challenge, some researchers have employed dynamic finite element methods (Al-Rifaie et al., 2017; Wang et al., 2019). However, these approaches still encounter meshing challenges.

1.2. *The discrete element approach*

The DEM, especially the spherepacking-based DEM (Cundall and Strack, 1979), offers attractive advantages in handling contact problems and eliminates the need for mesh discretization. The DEM has been utilized to examine porous materials, frequently employing a random spherepacking algorithm (Bakhshian and Sahimi, 2016; Huang et al., 2021; Duan et al., 2021). In these investigations, random spherepacking models were implemented, with spheres placed randomly within a predefined domain and following a specific radius distribution. The spaces between the spheres represented the pore spaces of the porous media. This approach was used to study changes in permeability, porosity, and relative permeability, albeit with a limited number of samples (Lin et al., 2022; Sun et al., 2013). To the best of the authors' knowledge, there are few papers addressing morphological changes under deformation of porous media, aside from porosity. Additionally, the random spherepacking model does not accurately reflect the true morphological characteristics of porous material samples.

Building DEM models to accurately capture irregular shapes is a challenging task, for which the clustering of spheres has become the most popular approach. Specifically, the spheres can be clustered following different strategies, such as the surface-based method, the voxel-based method, and the stochastic method. From the application perspective, DEM models that can represent real-shape particles have been widely used to simulate the mechanical behaviour of granular assemblies, such as railway ballast, sands, gravel materials, polymer–crystal composite particles, concrete, and Luna soil particles (Ferellec and McDowell, 2010; Lu and McDowell, 2007; Luo et al., 2011; Hu et al., 2021; Wang et al., 2020; Zhang et al., 2021; Matsushima et al., 2009).

The surface-based method creates the mesh and vertices on the surface of the particles and then creates a cluster of spheres based on the vertices. For example, the commercial software PFC3D can automatically create clumps of spheres to represent objects with irregular shapes (Taghavi, 2011) based on the mid-surface algorithm. This method constructs a triangulated surface through Delaunay tetrahedralization, and defines clusters using the centres and radii of the circumscribed spheres of each tetrahedron. Similarly, Ferellec and McDowell (2008) presented an overlapping multisphere clump method, where the spheres were created by expanding the tangent sphere along the normal inward direction of the vertices on the surface of particles. Matsushima and Saomoto (2002) introduced a dynamic optimization algorithm using primitive sphere elements to approximate complex grain shapes through a virtual time-marching scheme. This method ensures accurate grain shape representation by dynamically adjusting the sizes and positions of these spheres in response to a calculated virtual force from the surface vertice, optimizing the fit to the target grain's surface.

The voxel-based methods bypass the need to identify the surface of particles, by generating spheres directly from the pixel or voxel of the particles in 3D digital samples. Examples include Hagenmuller et al. (2015) and You et al. (2009), where small spheres were positioned at each voxel. This technique yields an accurate grain shape, but it also results in a high quantity of spheres. To address this issue, various methods have been developed to substitute small spheres with larger ones. In Wang et al. (2007) and Fu et al. (2010), small spheres were initially positioned on each voxel, and subsequently replaced by larger spheres using the Burn Algorithm, which can decrease the sphere count by 90%. Mede et al. (2018) devised a method based on the medial axis, where spheres of varying radii were positioned at voxels according to a distance map, followed by the application of a media surface filter and a reduction in spheres. The cluster formed by the medial axis-based method always exhibits flaws between two large spheres at the medial axis.

Some researchers have used a stochastic process to create clusters of spheres with different shapes, which have similar morphology to real particles (Lu and McDowell, 2007). This type of methods create new shapes rather than copying the shape from real particles.

In addition to the aforementioned strategies for generating clusters of spheres to replicate real-shape particles, researchers have also developed various mathematical frameworks to construct discrete elements with arbitrarily complex geometries that approximate real shapes. Among these, the Level-Set DEM (LS-DEM) (Kawamoto et al., 2016; Tahmasebi, 2018) employed a level-set function to represent the contours of particles from 3D binary images, from which a corresponding DEM model was formulated with the nodes arbitrarily positioned on the particle surfaces. Similarly, the Signed Distance Field (SDF) approach employed a comparable strategy for packing discrete and irregular particles (Lai et al., 2022). Furthermore, Capozza and Hanley (2021) proposed a hierarchical, spherical harmonic-based method for simulating irregularly shaped particles in DEM. This method used two distinct harmonic functions: a coarse one for identifying particle contact and a fine one for detailing the contacted surface. These advanced DEM approaches differ significantly from the spherepacking-based DEM in both element representation and contact formulation.

1.3. The contribution of this work

This study uses micro-CT images and DEM simulations to analyse the transport and morphology properties of rocks under compression stress. Based on micro-CT images, we construct high-fidelity spherepacking-based DEM models capable of accurately representing the morphological characteristics of practical porous media. Unlike previous real-shape DEM models, which build real-shape particles before assembling porous media geometry, our method directly processes system-level morphology, resulting in broader applicability and enhanced accuracy. The performance of our proposed DEM models is directly controllable through three algorithm parameters, making them more robust and flexible compared to existing CT-image based DEM models. Following rigorous validation against the FEM approach, our DEM model is applied to various rock samples to investigate properties such as permeability, porosity, tortuosity, specific surface area, and fractal dimension. Valuable insights are gained regarding how the transport and morphology properties of porous media react to stress and deformation. As far as the authors are aware, this research might be the first to investigate the trends in morphological characteristics under varying strains, and the first to present hundreds of simulation results for porous media subjected to compression deformation. Our image-based DEM approach is versatile and readily applicable to investigate other strain-sensitive properties of porous media.

The rest of the paper is organized as follows. Section 2 outlines the fundamental framework of spherepacking-based DEM, explaining the new algorithm for constructing high-fidelity DEM models from 3D binary images. Section 3 discusses the sensitivity analysis of the algorithm parameters, after which Section 4 validates our proposed DEM approach with FEM results. In Section 5, the image-based DEM method is deployed to investigate the strain-sensitive properties of porous media. Finally, Section 6 summarizes the concluding remarks.

2. Numerical method and model construction

2.1. Discrete element method

The spherepacking-based DEM conceptualizes objects as collections of particles with ideal shapes (disks in 2D; spheres in 3D), each obeying Newton's laws of motion (Cundall and Strack, 1979). The interaction between particles is governed by the force–displacement law of virtual spring contact models, with the optional insertion of bonds to impart tensile and shear strength.

The DEM employs a dynamic explicit scheme, assuming constant velocities and accelerations within each time step. A sufficiently small time step ensures disturbances propagate only to immediate neighbouring particles.

In this work, we adopt a parallel bond contact model (Potyondy and Cundall, 2004) for the initial contact between particles, and a linear contact model for the spheres-wall contact and any new contact created during compression. The parallel bond contact model facilitates the translation of force and moment between particles, and we change it to a linear contact model when the force between particles exceeds the tensile or shear strength.

$$\mathbf{F} = \mathbf{F}_s + \mathbf{F}_d + \mathbf{F}_n \tag{1}$$

$$\mathbf{M} = \mathbf{M}_t + \mathbf{M}_b \tag{2}$$

The force components include the normal force $\mathbf{F}_n$, the shear force $\mathbf{F}_s$, and the dashpot force $\mathbf{F}_d$. Moment components comprise twisting $\mathbf{M}_t$ and bending $\mathbf{M}_b$. At each time step, force and moment are updated per force–displacement law:

$$\mathbf{F} := \mathbf{F} + k\Delta\delta \tag{3}$$

$$\mathbf{M} := \mathbf{M} + k\Delta\theta \tag{4}$$

where k represents force or moment stiffness, and $\Delta\delta$ is the relative displacement or rotation increment. Tensile strength σ_c and shear strength τ_c are assessed to determine bond breakage. Acceleration is assumed constant over sufficiently small time steps.

The linear contact model can be described as two springs normal to the contact surface between particles. They do not resist relative rotation and tension, and slip is accommodated by imposing a Coulomb limit on the shear force. The parallel bond contact model contains two groups of mechanical components: the first is the same as the linear contact model, and the second is the parallel bond which resists relative rotation and tension when it is bonded. When the strength limit is exceeded, the bond breaks and it carries no load. The unbonded parallel bond model behaves as a linear contact model, see Fig. 1. During each time step, should the separation between two spheres, which previously had no contact, reduce to below the preset critical surface gap g_c, a new linear contact model is established between them.

The symbols in Fig. 1 and their respective values employed in this study are outlined in Table 1. The spring stiffness within the contact models can be derived from the corresponding Young's modulus, $k_n = EA/L$, where A denotes the contact area between two spheres, and L denotes the distance between the central points of two spheres. The shear stiffness can be calculated by $k_s = k_n/k^*$. It is noted that the actual dimensions of physical specimens, at 0.25 mm, are not mirrored in the numerical model; instead, a significantly larger scale of 100 m is utilized. The micromechanical parameter used in this study comes from the example of rock test from the PFC3D document. The original case study was a uniaxial compression test of rock samples. The original samples have the macroscopic Young's modulus as 4.5 GPa, with uniaxial compression strength of 33.9 MPa. The original sample is 10 cm long and 5 cm in diameter, conforming to typical laboratory core samples. The radius of spheres are uniformly distributed between 1.0e−3 m and 1.5e−3 m. In the simulation of this paper, some parameters were changed. The effective Young's modulus is relatively small, at 2 MPa, as opposed to the typical 2 GPa found in the example. This length-scale difference and the reduced effective Young's modulus yield a diminished Young's modulus at the macroscopic level, and they lead to substantially larger time steps, thereby reducing simulation time. Moreover, the tensile strength and cohesion are relatively large, ensuring an extended elastic phase.

In FEM models, material properties such as stiffness and strength are directly determined via laboratory tests. However, the DEM model captures macroscopic material behaviours through microscopic particle–particle interactions, and the associated constitutive properties are not readily measurable via standard laboratory tests. DEM models typically rely on geometric parameters, such as particle size distribution and particle count ratios, alongside microscopic mechanical parameters like virtual spring stiffness and tensile strength. To initiate a DEM simulation, geometric parameters are initially defined, followed by calibration of mechanical parameters against experimental data. While the relationship between DEM parameters and material properties is straightforward for simple packing configurations, complex scenarios with arbitrary particle arrangements require a calibration process. During this process, DEM simulations are adjusted to align with material properties observed in experimental tests.

2.2. CT-image based DEM model

To build high-fidelity DEM models for porous media based on their micro-CT images, it is crucial to accurately capture the heterogeneous microstructure with a well-designed ensemble of discrete elements.

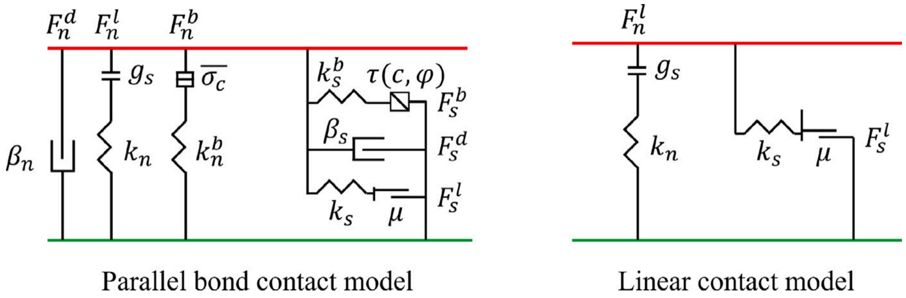

Fig. 1. Components of the parallel bond contact model and linear contact model.

Table 1
The parameters for DEM numerical model.

Symbol	Description	values
Parallel bond contact model		
Parallel bond group		
E_b	Effective Young's modulus of bond [Pa]	2e6
k_b^*	Normal-to-shear stiffness ratio, $k_b^* = k_n^b/k_s^b$	1.0
$\overline{\sigma_c}$	Tensile strength [Pa]	40e7
c	Cohesion [Pa]	50e7
ϕ	Friction angle [degree]	0
Linear group		
μ	Friction coefficient, μ	0.577
E_l	Youngs' modulus of linear spring [Pa]	2e6
k_l^*	Normal-to-shear stiffness ratio	1.0
g_s	Critical surface gap between spheres [m]	0.1
Damp group		
β_n	Normal critical damping ratio	0.5
β_s	Shear critical damping ratio	0.5
Linear contact model		
E	Young's modulus of linear spring [Pa]	2e6
k^*	Normal-to-shear stiffness ratio, $k^* = k_n/k_s$	1.0
μ	Friction coefficient	0
g_s	Critical surface gap between spheres [m]	0.1
Spheres		
density	Density of spheres [kg/m^3]	2700

$k_n = EA/L$, where A is the contact area between spheres, L is the distance between central points of spheres.
$k_s = k_n/k^*$, as well as k_s^b.

Although random spherepacking is commonly adopted in previous DEM models, it does not capture the real morphological features of porous media.

This paper adopts a voxel-based approach to constructing the DEM model of porous media from micro-CT images. This concept has been used in building real-shape grains/particles in porous media and it has also been applied to build pore networks, where the focus is on pore space rather than the solid phase (Arand and Hesser, 2017; Silin and Patzek, 2006; Mede et al., 2018). The method takes binary images obtained from CT scans as inputs and produces an assembly of spheres that represents the geometry of the sampled media. Specifically, the process involves three steps: creating a distance map, generating spheres, and removing redundant spheres. A 2D example of this process is shown in Fig. 2.

The binary images, as input (upper left image in Fig. 2), use coordinates $x \in \mathbf{N}^3$ to index the voxels. Each voxel is assigned a value: $f(x) = 1$ for solid and $f(x) = 0$ for void. Subsequently, a new matrix D, mirroring the input image's dimensions, is constructed. The values in D represent the distance field of the input images, indicating the distance to the nearest void voxels. The values in the void voxels are 0, and those in the solid voxels start from 0.5 and increase in increments of 0.5, where the value 0.5 indicates a face-to-face connection with a void voxel (upper right image in Fig. 2).

Based on the distance matrix D, the radii of the spheres corresponding to each solid voxel are determined. The radius of a specific voxel is equal to the nearest integer of the corresponding value in D minus 0.5. This results in a new array [radius, x], which facilitates the construction of a DEM model for numerical simulation (lower right image in Fig. 2).

The final step involves reducing redundant spheres. A model constructed with all spheres retains the maximum geometric information from the digital rock samples, but requires extensive computational resources. For example, a model from a cubic rock sample with a 100^3 resolution may contain about 700,000 spheres, which is impractical for DEM simulation. Thus, a criterion to reduce overlapping spheres was introduced:

$$R_A - R_B + \epsilon R_B - dist(A, B) \leq 0 \tag{5}$$

where $\epsilon \geq 0$ is a relaxation parameter, allowing sphere B to slightly bulge out of sphere A while still being considered contained. Tuning ϵ adjusts the extent of this bulge, reducing the total number of spheres in the model. Fig. 3 depicts three scenarios with different ϵ values. With $\epsilon = 0$, the base sphere absorbs only those spheres entirely within it; with $\epsilon = 1$, it removes spheres whose centres fall within its area; and with $\epsilon = 2$, it eliminates any sphere overlapping with it.

Algorithm 1 describes the criterion and procedure for reducing redundant spheres. Initially, two groups of spheres are established: the group $\{R\}$ encompasses all spheres formed up to this point and the group $\{U\}$ is an empty set. The largest spheres from $\{R\}$ are then selected and transferred to $\{U\}$. All remaining spheres in $\{R\}$ are examined, and any spheres deemed to overlap based on the criterion (5) are eliminated. This procedure is repeated until only the smallest spheres ($r = 0.5$) remain in $\{R\}$. These smallest spheres, with a radius of 0.5, can only touch each other without any overlap. These remaining smallest spheres are then moved to the set $\{U\}$. Finally, the set $\{U\}$ contains all the necessary spheres.

Algorithm 1 Sphere Reduction Algorithm

```
Initialize sets ${R}$ and ${U}$. ${R}$ includes all spheres, ${U}$ is a null set.
repeat
    Select the largest sphere from ${R}$, denote this sphere as $R_A$.
    Move $R_A$ from ${R}$ to ${U}$.
    for all $R_B$ in ${R}$ do
        if $R_A - R_B + \epsilon R_B - dist(A, B) \leq 0$ then
            Remove $R_B$ from ${R}$.
        end if
    end for
until $R_A$ is the smallest sphere with a radius of 0.5
${U}$ includes all spheres used to construct the model.
```

2.3. Model parameters and test cases

The DEM model construction is controlled by three algorithm parameters, which affect both geometric and mechanical characteristics. The relaxation parameter ϵ manages the sphere overlap; the maximum sphere radius $R_{\max}$ ensures that spheres exceeding this limit are resized to $R_{\max}$; the minimum radius parameter $R_{\min}$ filters out spheres falling

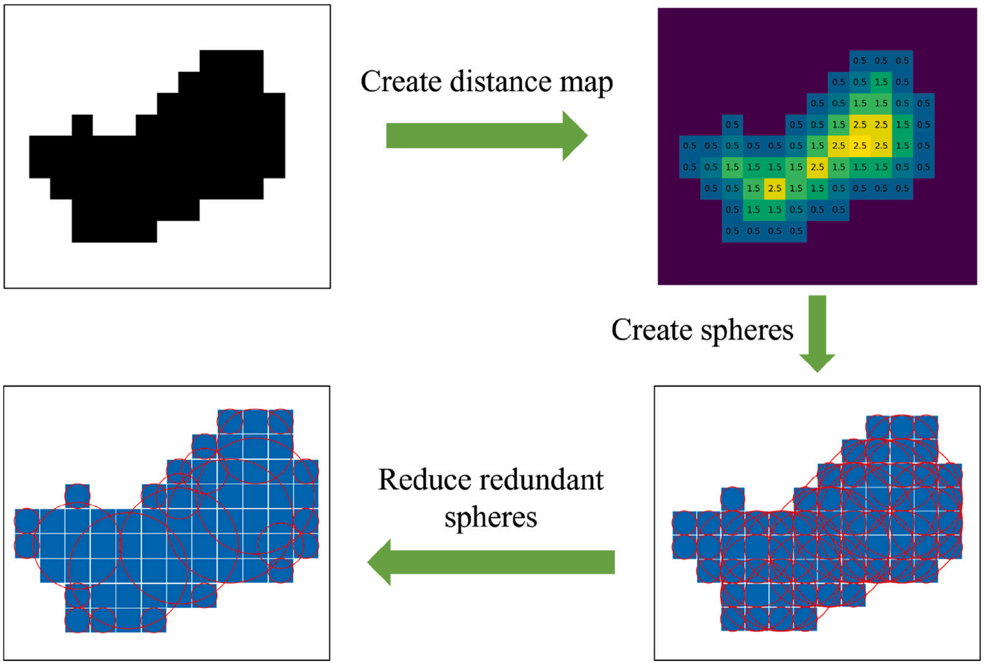

Fig. 2. Construction of the CT-image-based DEM model.

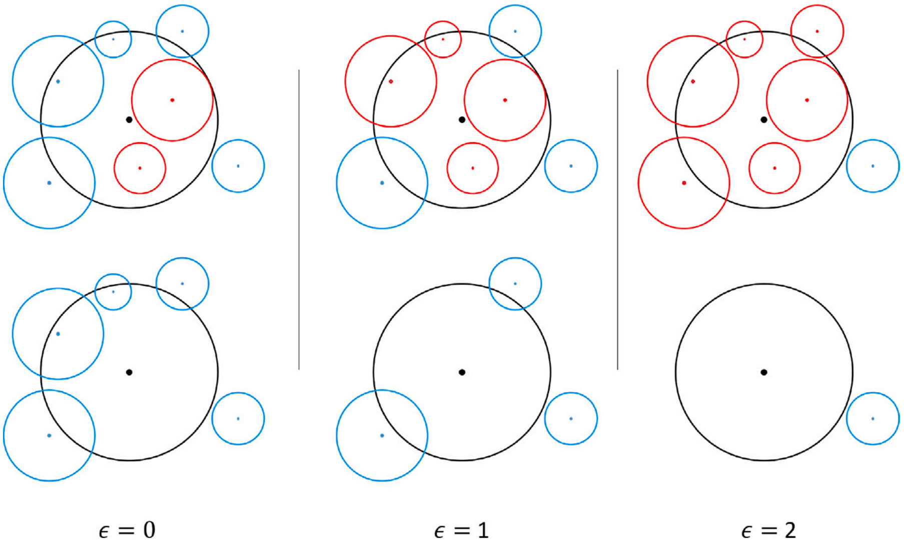

Fig. 3. Influence of ϵ. The black sphere is the reference. Red spheres are to be removed, while blue spheres will remain. The top row shows spheres before removing redundancies, and the bottom row shows the result after removal.

below this threshold. Nine cubic digital rock samples with varying morphology features are employed to analyse the performance of algorithm parameters ϵ, $R_{\max}$ and $R_{\min}$. As shown in Fig. 4, each sample contains 100 × 100 × 100 voxels, and each voxel represents a scale of 2.5 μm. These nine cases are obtained from Digital Rocks Portal online library (Neumann et al., 2020). The parameter analysis starts with the relaxation parameter ϵ, which is varied from 0 to 2.0 in increments of 0.1. These 21 ϵ values are applied across the nine test cases. Subsequently, the effects of $R_{\max}$ and $R_{\min}$ are checked for $R_{\max} = 100, 15, 10, 5$ and $R_{\min} = 1, 2, 3$.

As previously discussed, the mechanical properties of materials are influenced by the geometry and characteristics of their microcomponents. Unlike the FEM, the DEM necessitates an inverse process to ascertain the mechanical properties of micro-constituents. Initially, the parameters' effects on the geometry of the models are analysed, utilizing the total sphere count as a key efficiency indicator. Then, the impact of the parameters on macroscopic mechanical behaviour is assessed using constant microscopic constituents, with Young's modulus serving as the primary index. This approach provides insights for selecting microscopic mechanical parameters tailored to specific geometries. Finally, an index is introduced to quantify the discrepancy between the original binary images and their reconstructed counterparts in the DEM model. This index helps to evaluate how effectively the DEM model preserves the geometry of the physical samples.

3. Testing results and analysis

3.1. Influence on the total number of spheres in a model

3.1.1. The influence of ϵ

The relaxation parameter ϵ is varied from 0 to 2, in intervals of 0.1. Fig. 5 illustrates the variation in the average total number of spheres

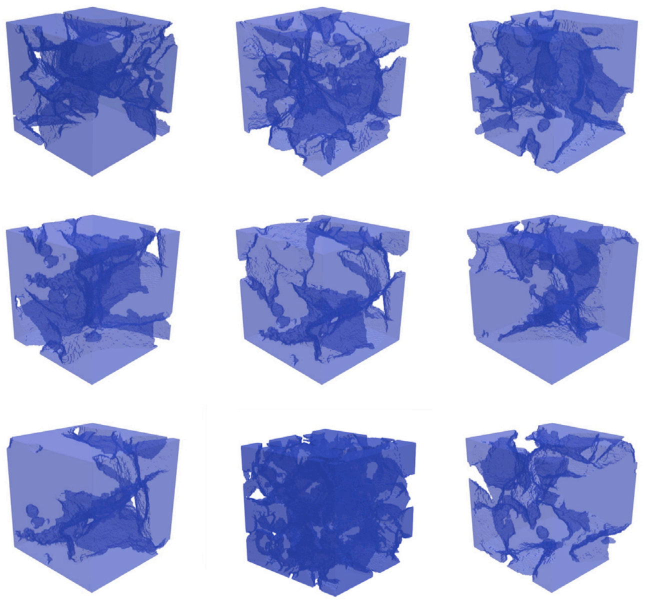

Fig. 4. Nine cases used in the model parameter analysis.

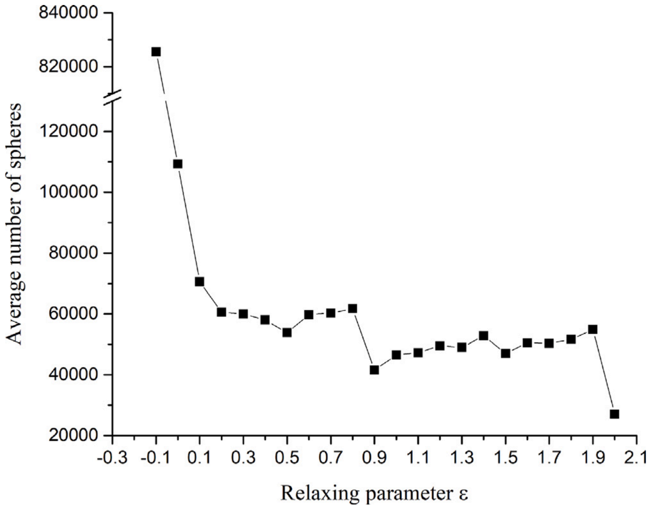

Fig. 5. The average numbers of spheres of 9 cases with different ϵ (The value at -0.1 denotes the number of spheres before the operation).

across nine cases as a function of ϵ, without constraints on $R_{\max}$ and $R_{\min}$. The data reveals an overall downward trend in the total number of spheres, interspersed with periodic fluctuations. Notably, there is a sharp decline in sphere count for $\epsilon < 0.3$, with distinct decreases observed at ϵ values of 0.5, 0.9, 1.5, and 2.0. At other intervals, the trend is less predictable, showing slight increases in sphere count with increasing values of ϵ.

This operation has a significant impact on the elimination of redundant spheres. Interestingly, even at $\epsilon = 0$, the number of spheres is reduced from over 800,000 to approximately 100,000. This count further declines to around 50,000 at $\epsilon = 0.5$ and approximately 40,000 at $\epsilon = 0.9$, representing a mere 5% of the original number. As ϵ reaches 2.0, the sphere count reduces to a mere 20,000, highlighting the efficacy of the method in optimizing the model's complexity.

3.1.2. The influence of the maximum radius R_{max}

The maximum radius $R_{\max}$ significantly impacts the number of spheres within the model, with larger spheres potentially being replaced by several smaller ones. This parameter also influences the mechanical properties of the DEM model, including aspects like Young's modulus and compression strength. To investigate the effects of $R_{\max}$, four distinct values are examined: 100, 15, 10, and 5. These cases are respectively referred to as MAX100, MAX15, MAX10, and MAX5. The condition $R_{\max} = 100$ effectively represents an absence of radius limits, as this value exceeds the largest sphere radius present in our models.

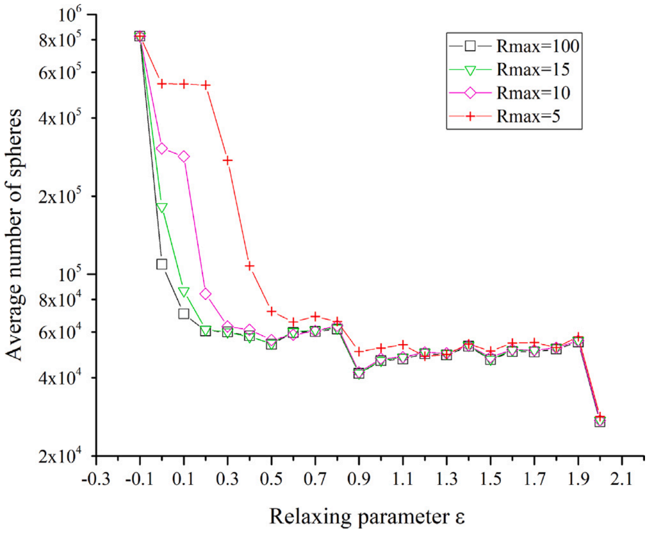

Fig. 6. The number of spheres with different limits with respect to ϵ ($R_{max} = 100$ denotes no limits).

Fig. 6 illustrates the variation in the average number of spheres as a function of the relaxation parameter ϵ under different $R_{\max}$ limits. The constraint on maximum radius notably increases the total number of spheres, particularly when $R_{\max}$ is reduced to below 15. The impact of $R_{\max}$ is more pronounced at smaller ϵ values, with the differences diminishing as ϵ increases. Specifically, at $\epsilon = 0$, the sphere count in the MAX5 case only decreases to about 600,000, approximately 300,000 in MAX10, and nearly 200,000 in MAX15—significantly higher than in the MAX100 case. As ϵ is adjusted to 0.2, the number of spheres in MAX15 aligns with that in MAX100. The sphere counts in MAX10 reach a similar level as MAX100 at $\epsilon = 0.5$ and MAX5 when ϵ exceeds 1.2. Interestingly, the number of spheres for different $R_{\max}$ settings tends to converge at an ϵ value of around 1.9.

An interesting phenomenon is that when $R_{max} = 5$, the total number of spheres does not change when the ϵ value changes from 0 to 0.2. When $R_{max} = 10$, the total number of spheres only decrease a little when epsilon changes from 0 to 0.1. When $\epsilon = 0$, the DEM model has a set of regularly arranged spheres, with radii of 0.5, 1.5, 2.5, 3.5, and 4.5. The distance between each sphere is at least 1 unit. Only when $\epsilon = 0.3$, and $R_b = 3.5\, or\, 4.5$, the criterion $R_a - R_b + \epsilon \times R_b$ would get values of 1.05 and 1.35, which are larger than $\mathbf{distance}(A, B) = 1$, by which the new removing operation gets activated.

Fig. 7 provides a visualization of the distribution of sphere radii under different $R_{\max}$ values, with the data from Case 9. Regardless of the chosen $R_{\max}$, there is a significant drop in the number of the smallest spheres as ϵ increases from 0. Subsequently, as ϵ continues to grow, the count of smaller spheres begins to rise. Conversely, the number of larger spheres decreases as the relaxation parameter ϵ increases. Notably, in the case of the natural condition ($R_{\max} = 100$), certain radii of spheres become entirely absent at $\epsilon = 0$ and then reappear as ϵ undergoes variation.

For a more direct visualization of the impact of ϵ and $R_{\max}$, please refer to Fig. 8, which provides cross-sectional views of the DEM model constructed around the maximum sphere. These images offer insights into the model's internal structure. Notably, as ϵ increases, the outer surface of the model transforms. It becomes increasingly rugged, with

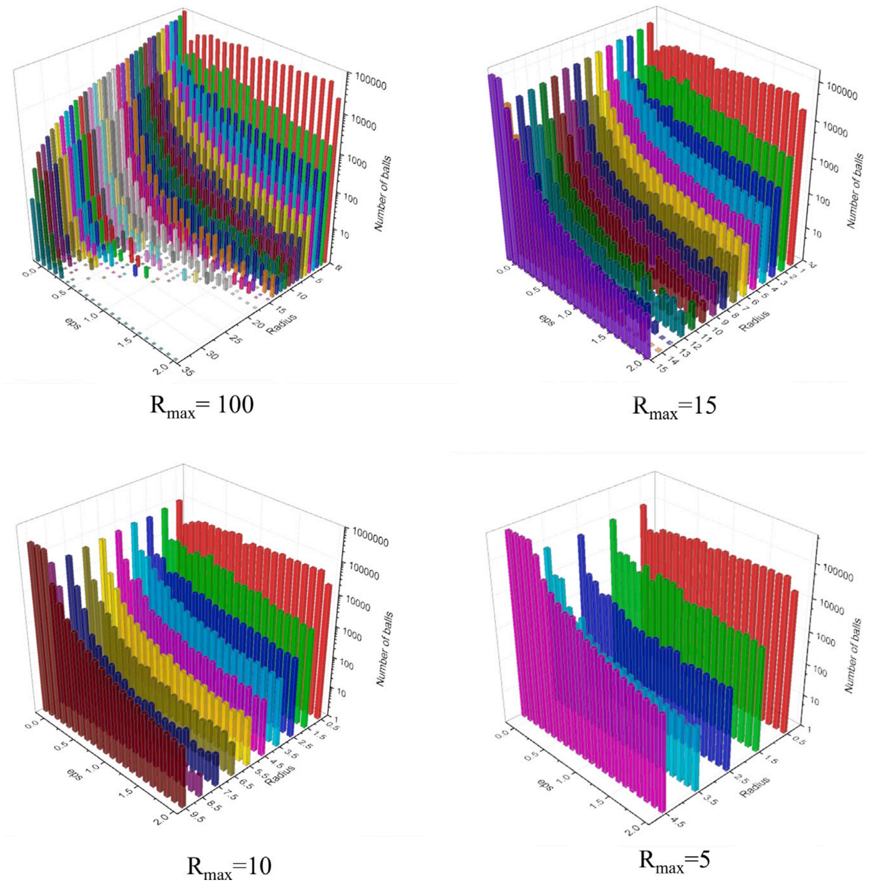

R_{max}= 100 R_{max}=15

R_{max}=10 R_{max}=5

Fig. 7. The radius distribution under different limits (R_{max} = 100 denotes no limit).

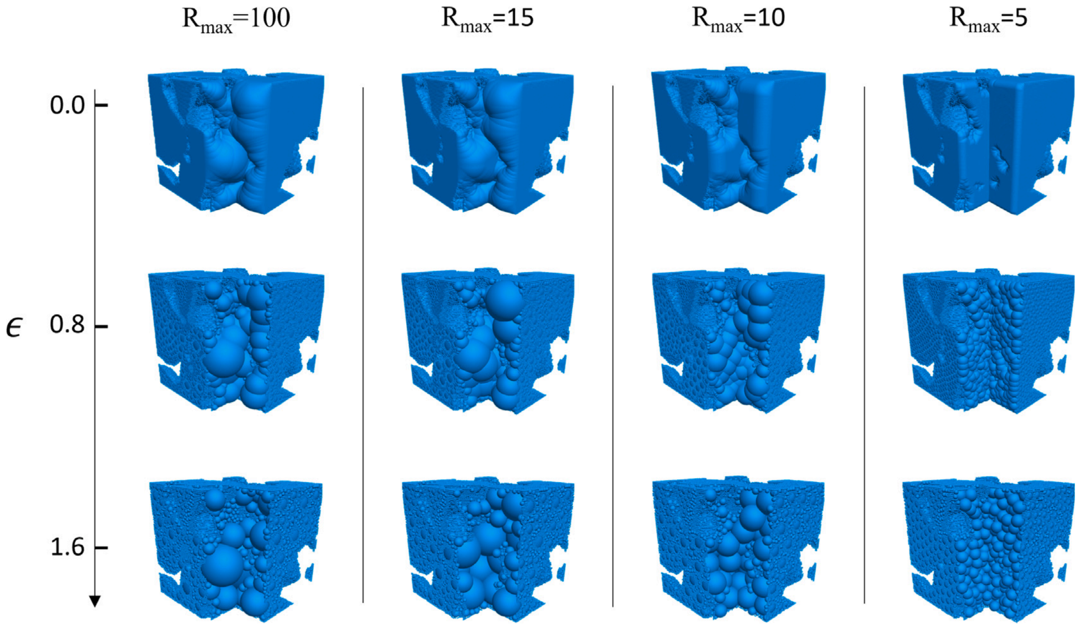

Fig. 8. The DEM models with different ϵ and different limits of maximum radius (R_{max} = 100 denotes no limit).

a noticeable reduction in sphere overlap. Initially, the outer surfaces are predominantly composed of highly overlapped large spheres. However, as ϵ continues to rise, these larger spheres are gradually replaced by smaller spheres with reduced overlap.

In this test case, we have primarily focused on using smaller R_{max} values to enhance the accuracy of our simulations, especially when compared to the fine mesh approach of the FEM. Smaller spheres with reduced R_{max} values allow us to capture finer details and deformations within the porous media, providing a more comprehensive representation. It is noted that in certain research scenarios, granular porous media can be segmented into smaller grains using specific methods. This segmentation process can help determine the appropriate R_{max}

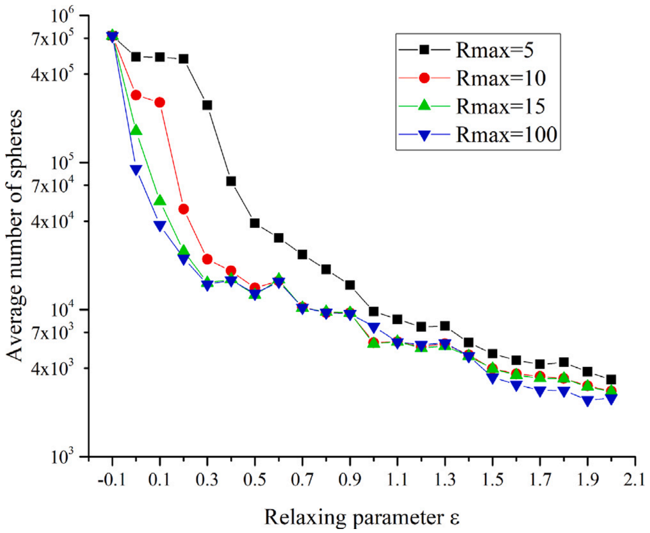

Fig. 9. The number of spheres with different limits with respect to ϵ, the smallest spheres were removed ($R_{min} = 1$).

values for spheres within the model, tailored to the characteristics of the material being simulated.

3.1.3. The influence of the minimum radius R_{min}

The analysis of sphere size distribution reveals that spheres with the smallest radius of 0.5 constitute a significant portion of the total number of spheres. Moreover, the number of these smallest spheres increases with the relaxation parameter ϵ, as shown in Fig. 7. Removing these smallest spheres represents an effective strategy for improving simulation efficiency. Notably, our method primarily positions these small spheres at the model's outer surface, making their removal an acceptable approach for reducing the total number of spheres.

To examine the impact of $R_{\min}$ more closely, Fig. 9 illustrates the change in the total number of maximum spheres when the smallest spheres are excluded. This exclusion leads to a smoother decrease in the number of spheres compared to the trend depicted in Fig. 6.

Fig. 10 gives a more clear insight on how the number of smallest spheres changes with ϵ. The image shows a similar but contrary periodic change in the total number of spheres. The number of smallest spheres falls when ϵ is equal to 0.5, 0.9 and 2.0.

To gain insight into this issue, a simplified 2D model was employed in our study. Fig. 11(a) illustrates the total number of spheres as it changes with varying ϵ, while Fig. 11(b) presents the trends for both the smallest spheres and the larger spheres. The observed periodicity arises from alterations in the smallest spheres' configuration.

To provide a more detailed comparison, the conditions of $\epsilon = 0.2$ and $\epsilon = 0.3$ are selected for analysis. As ϵ varies from 0.2 to 0.3, several notable changes occur: the total number of spheres and the count of smallest spheres increase, while the number of larger spheres decreases. Fig. 12 displays the differences between these two stages. The numbers within red squares denote spheres with specific radii that exist in one stage but are removed in the other. It is evident that in the $\epsilon = 0.2$ stage, most of the red squares are concentrated in the central area. Conversely, when $\epsilon = 0.3$, the red squares are located at the edge. Furthermore, the number of spheres with radii smaller than 7 increases while the remaining spheres become less numerous, with the largest sphere remaining unchanged.

The solution to this issue appears to be associated with the removal of an increasing number of middle-sized spheres as ϵ is raised. This, in turn, leads to the preservation of smaller spheres. In Fig. 13, we use a black sphere to represent a large sphere as a reference, a red sphere to denote a middle-sized sphere that will be removed as ϵ increases, and a blue sphere to signify the smallest sphere, which is retained as ϵ grows.

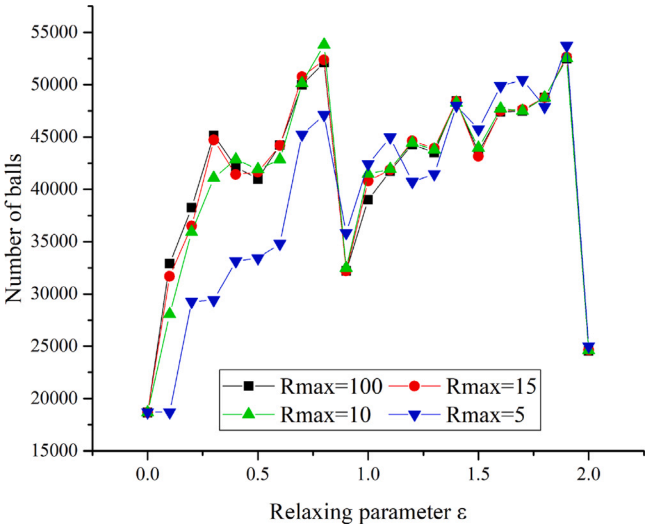

Fig. 10. The number of smallest sphere with different ϵ and different limits of maximum radius (Rmax = 100 denotes no limit).

Table 2
Young's modules of different parameter combination (GPa).

	$\epsilon = 0.4$	$\epsilon = 0.6$	$\epsilon = 0.8$	$\epsilon = 1.0$	$\epsilon = 1.2$	$\epsilon = 1.4$	$\epsilon = 1.6$	$\epsilon = 1.8$
$R_{max} = 5$	1624	609.5	306.1	111.5	52.63	33.13	20.52	12.04
$R_{max} = 10$	756.2	320.3	145.78	65.75	41.71	28.01	19.63	12.70
$R_{max} = 15$	584.03	236.3	107.8	52.66	34.69	26.15	18.42	10.77
$R_{max} = 20$	513	191.2	87.6	45	30.7	23.04	17.2	11.64

3.2. The parameters' influence on Young's modulus

As discussed earlier in Section 2.1 and Section 2.3, to determine the microscopic mechanical parameters in DEM models requires an inverse process based on the given geometry and macroscopic mechanical parameters. To investigate the parameters' influence on Young's modulus, DEM models are constructed using different combinations of control parameters: ϵ, R_{max}, and R_{min}, and each model undergoes a uniaxial compression simulation of the same settings. The uniaxial compression simulations were performed by simply moving the top wall downward and keeping the bottom wall fixed. Young's modulus is then calculated according to the stress–strain curve obtained from the simulation results, $E = \frac{\text{stress}_2-\text{stress}_1}{\text{strain}_2-\text{strain}_1}$. All DEM models use consistent microscopic mechanical parameters, as detailed in Table 1, while the effective Young's modulus in this section were changed to the real scale, 2 GPa. During the simulation, the upper surface is assigned a velocity of 0.1 m/s to compress the sample, while the bottom surface remains fixed. Case 9 is chosen for illustration, and Fig. 14 shows the stress–strain curve from the simulation results with different ϵ values when $R_{max} = 15$ and $R_{min} = 1$.

The influence of the ratio between the particle size and the total number of particles on the macro-mechanical behaviour of DEM models is well-documented. Many researchers have studied the grain size effect in granular materials using these properties. Young's modulus values obtained from different combinations of the three parameters are presented in Tables 2 and 3. Notably, Young's modulus tends to decrease as the relaxing parameter (ϵ) increases, and models with larger R_{max} values generally exhibit smaller Young's modulus. A significant observation from the comparison of the two tables is that the removal of the smallest spheres results in a reduction in Young's modulus. The values of Young's modules are strongly related to the total number of spheres, which correlates with the number of contacts established in the DEM model. A larger number of spheres will result in a higher Young's modulus.

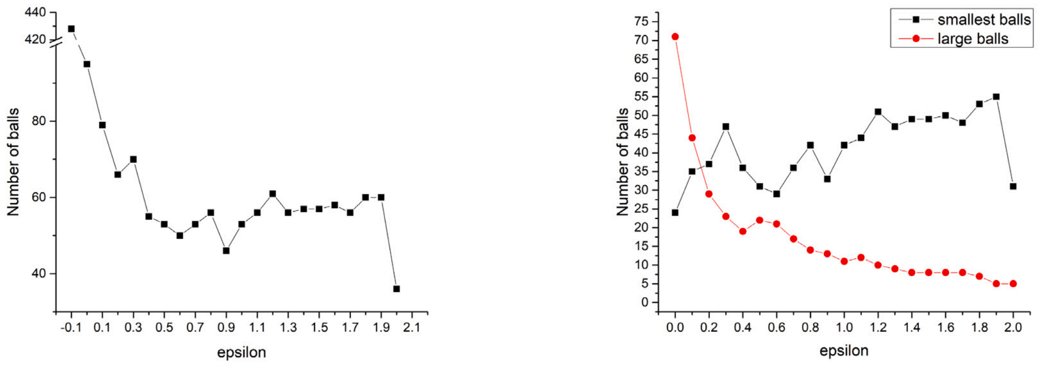

(a) Total number of spheres in 2D case (b) Smallest spheres and large spheres

Fig. 11. Number of spheres in 2D case.

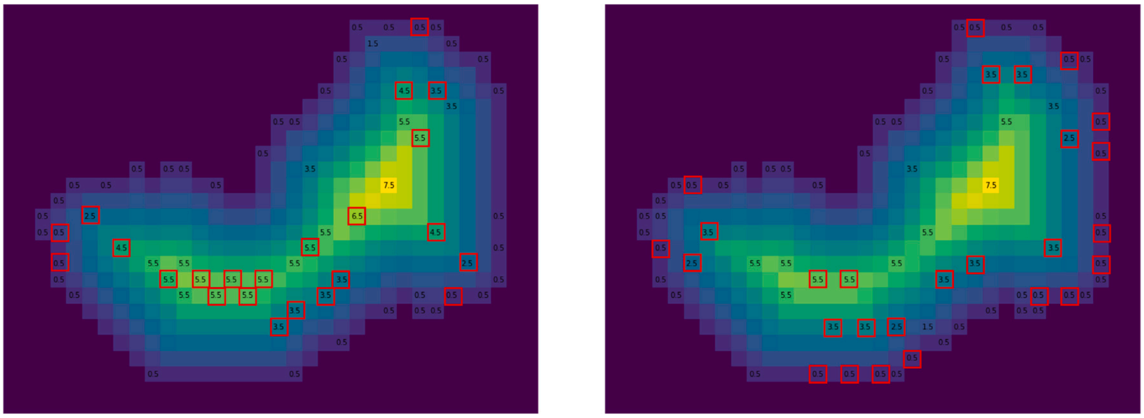

(a) $\epsilon = 0.2$ (b) $\epsilon = 0.3$

Fig. 12. Difference between two stages (red squares signed the differences).

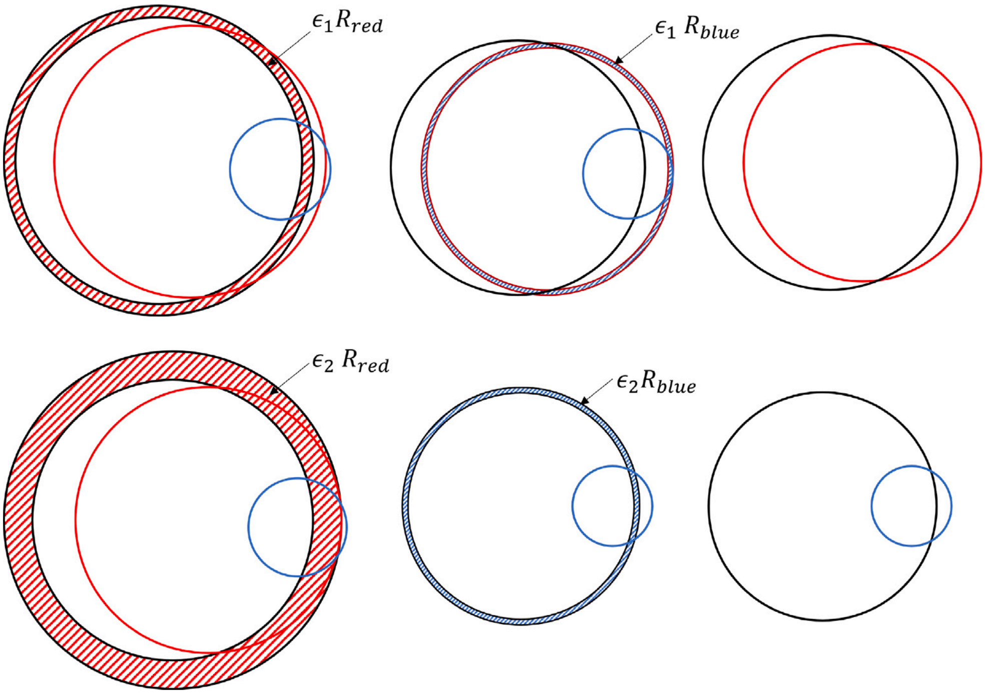

Fig. 13. Different results with different ϵ values.

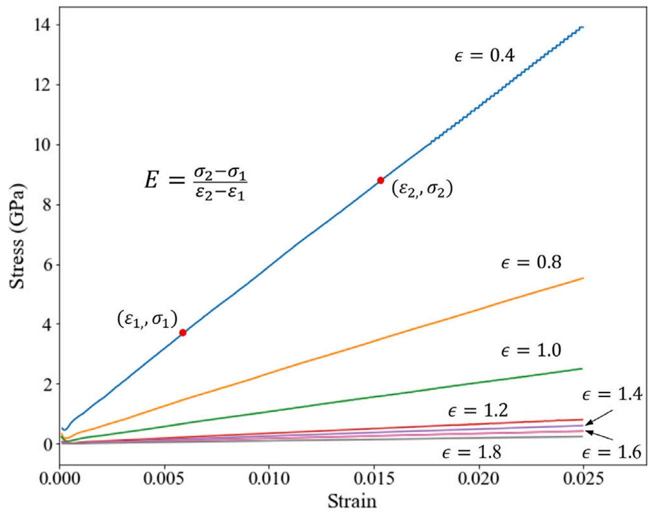

Fig. 14. The stress–strain curve from simulation results with different ϵ, when R_{max} = 15 and $R_{min} = 1$.

Table 3
Young's modules of different parameter combination when $R_{min} = 1$ (GPa).

	$\epsilon = 0.4$	$\epsilon = 0.6$	$\epsilon = 0.8$	$\epsilon = 1.0$	$\epsilon = 1.2$	$\epsilon = 1.4$	$\epsilon = 1.6$	$\epsilon = 1.8$
$R_{max} = 5$	1615.4	572.2	274	102.15	50.45	32.2	19.92	11.29
$R_{max} = 10$	700.1	297.2	130.97	62.28	39.30	26.07	18.47	11.84
$R_{max} = 15$	549.1	222	100.81	49.84	32.56	24.73	17.24	9.68
$R_{max} = 20$	482.9	180.2	82.93	43.13	29.04	23.26	16.11	10.6

3.3. Volume loss

In this case study, the volume loss is chosen to examine the influence of the three control parameters on DEM models. The volume loss gives the difference of volumes between the raw binary image and the reconstructed DEM model. The number of solid voxels in the original binary images presents the raw model volume, whilst the volume of the reconstructed DEM model is approximately evaluated via a Monte Carlo sampling process. The binary image has the resolution of 100 × 100 × 100 voxels, and the number of Monte Carlo sampling points is set as $5,000,000$.

As shown in Fig. 15, the volume loss grows with the increase of relaxing parameter ϵ and R_{min}, while the smaller R_{max} usually leads to larger volume loss. If 5% maximum volume loss is taken as a criterion to build DEM models, then the combination of $\epsilon = 0.9$ and $R_{min} = 1$ will ensure acceptable results for any R_{max} values. Likewise, under the same 5% volume loss constraint, if we set $\epsilon = 0.4$, then R_{min} can be allowed to up to 3.

4. Validation

To examine the performance of our proposed CT-image-based DEM models, a direct comparison with the FEM simulation is presented here. Specifically, three distinct morphological models are considered: a Face-Centred Cubic (FCC) model, a Body-Centred Cubic (BCC) model, and a porous media model extracted from a digital rock sample. As shown in Fig. 16, the DEM models are configured using relaxation parameter $\epsilon = 0.9$ and radius parameters $R_{max} = 4.5$ and $R_{min} = 1$. Our simulations replicate a uniaxial compression process, where the lower faces of the samples are immobilized, while the upper faces are subjected to controlled displacement. In the DEM configurations, the upper face is assigned a constant velocity of 0.01 voxel/s, and in the FEM simulations, the upper face experiences a pre-determined displacement. Owing to convergence challenges, the FEM simulations are conducted without contact detection, thus facilitating a direct comparative examination of the deformation in porous materials as modelled by both DEM and FEM. For simplicity, the simulations are confined to the elastic stage. The mechanical parameters used in the DEM simulation are the same as in Table 1. The Young's modulus and Poisson's ratio are 50 GPa and 0.3, respectively. All simulations are controlled by strain or displacement rather than stress.

4.1. FCC model

In the FCC unit cell structure, spheres are positioned at all corners of the lattice as well as at the centre of each cube face. Spheres located at the face centres are shared between two adjacent unit cells, with each cell incorporating half of these spheres. In our model, upon the application of compression, spheres positioned at the centres of the faces come into contact. This interaction is pivotal for understanding the mechanical behaviour of the FCC structure under compressive forces.

Fig. 17 illustrates the displacement contour map along the z-axis, captured under varying degrees of vertical compression (0.02, 0.04, and 0.1). The depicted cross-section, oriented parallel to the y–z plane, intersects the FCC model's central point. At a vertical strain of 0.02, only a quarter of the upper section of the model exhibits a displacement of less than 2 voxels, while the remainder of the FCC structure retains its original position. With the strain increased to 0.04, the spheres located at both the upper and middle faces display displacements of 2 and 4 voxels respectively, whereas those at the bottom face remain stationary. Notably, at a strain of 0.1, the DEM results indicate that the spheres have commenced contact, with those in the contact zone exhibiting differential displacements compared to their counterparts located further away. Conversely, in the FEM model, the absence of contact detection leads to the overlapping of elements in the contact area without affecting the displacement of surrounding elements. Fig. 18 presents a comparison of the simulation results from DEM and FEM for the FCC model. Four control points, labelled P1, P2, P3, and P4, are chosen to track their displacements along the z-axis. The initial coordinates of these points in the undeformed model are $(28, 50, 82)$, $(21, 50, 82)$, $(70, 50, 81)$, and $(77, 50, 65)$. P1 and P3 are part of the half spheres on the top side, while P2 and P3 are part of the half spheres on the left and right sides. For strains less than 0.08, these points move downward linearly. When the strain increases to approximately 0.1, contact occurs between the points. Consequently, P1 and P3 move downward more slowly due to resistance from P2 and P4. Meanwhile, the FEM results remain unchanged as FEM does not account for contacts in the simulation. This simulation outcome demonstrates substantial congruence between the DEM and FEM methodologies, thereby reinforcing the validity of our model.

4.2. BCC model

The BCC structure is characterized by a cubic unit cell in which spheres are positioned at each corner and at the centre of the cube. In this arrangement, every sphere is equidistantly surrounded by eight nearest neighbours located at the cube's corners. In our study, the spheres at the corners are slightly enlarged to facilitate easier contact with their opposite counterparts.

Fig. 19 presents the displacement contour map derived from both the DEM and FEM simulations, displaying the external surface of the model. At a strain of 0.02, only the upper half of the model exhibits displacement. As the strain increases to 0.04, the spheres on the top surface and at the centre point demonstrate noticeable displacement, with those at the top surface coming into contact with the spheres at the bottom surface. The results from the DEM and FEM are slightly divergent. In the DEM analysis, the displacements of elements are altered upon contact; the elements in the top spheres are counteracted by those in the bottom spheres. Displacements of elements in the top spheres near the contact area are smaller compared to those of other

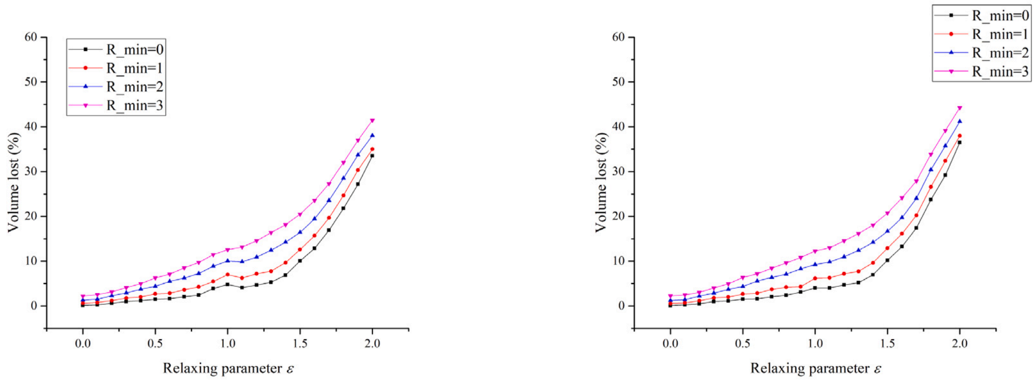

(a) $R_{max} = 20$ (b) $R_{max} = 15$

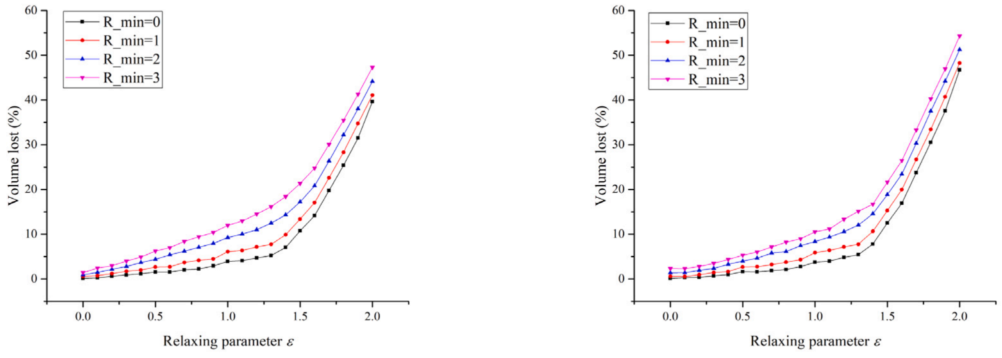

(c) $R_{max} = 10$ (d) $R_{max} = 5$

Fig. 15. Volume loss.

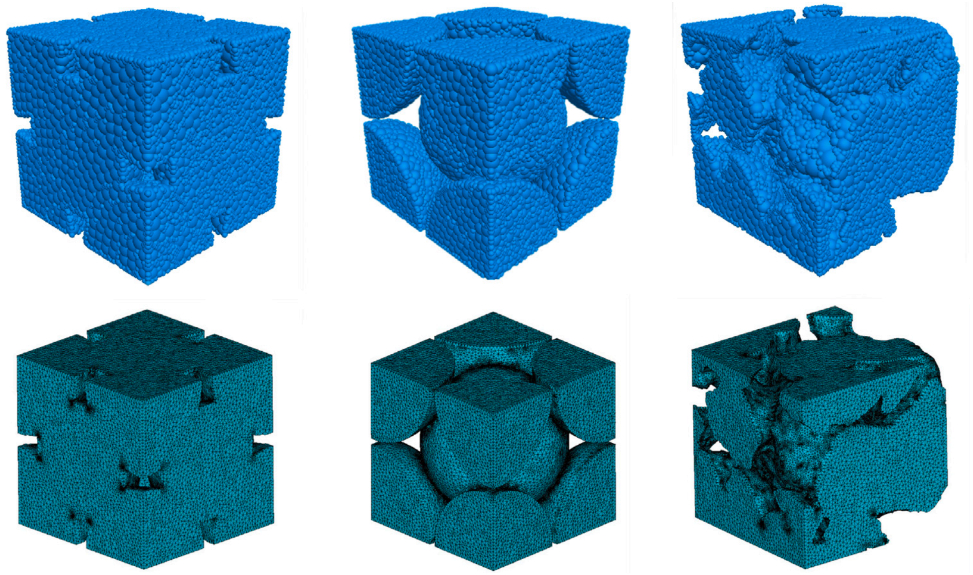

Fig. 16. Three different models. From left to right are FCC, BCC and Porous media; the top row is DEM models and the bottom row is FEM models.

spherical elements in the top spheres. Conversely, the contact area in the bottom spheres exhibits larger displacements than elements in other areas of the bottom spheres. In the FEM result the top spheres overlap with the bottom ones, and they exhibit a slight twist due to the absence of support from the bottom spheres. Overall, the trend in total displacement between the DEM and FEM simulations demonstrates substantial agreement. Fig. 20 illustrates the displacements of four control points obtained from DEM and FEM simulations of the BCC model. The positions of these points are depicted in the left image of the figure, representing the corner nodes expected to contact each other during compression. For strains below 0.02, points P1 and P3 in both DEM and FEM descend linearly at the same rate, while P2 and

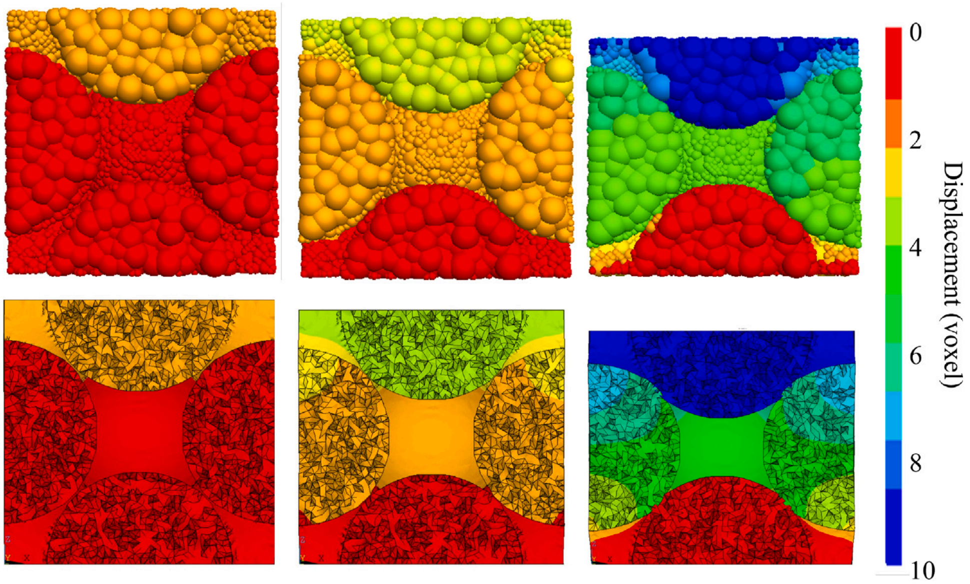

Strain = 0.02 Strain = 0.04 Strain = 0.1

Fig. 17. The simulation of FCC by DEM and FEM. The first row is DEM results, whilst the second row is FEM results.

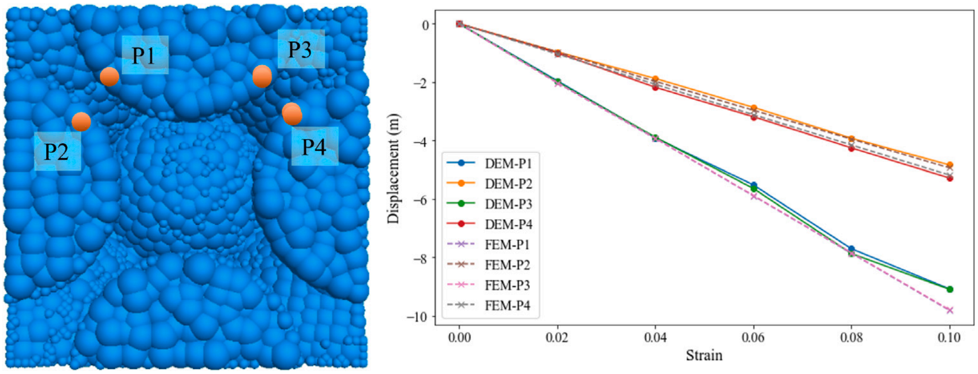

Fig. 18. The comparison of simulation results from DEM and FEM of the FCC model.

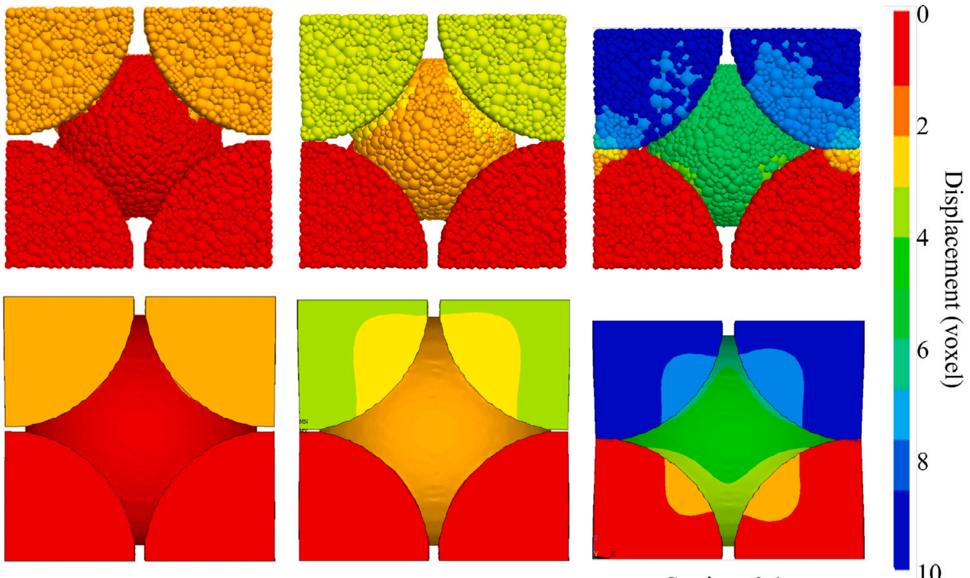

Strain = 0.02 Strain = 0.04 Strain = 0.1

Fig. 19. The simulation of FCC by DEM and FEM. The top row is DEM results, and the bottom row is FEM results.

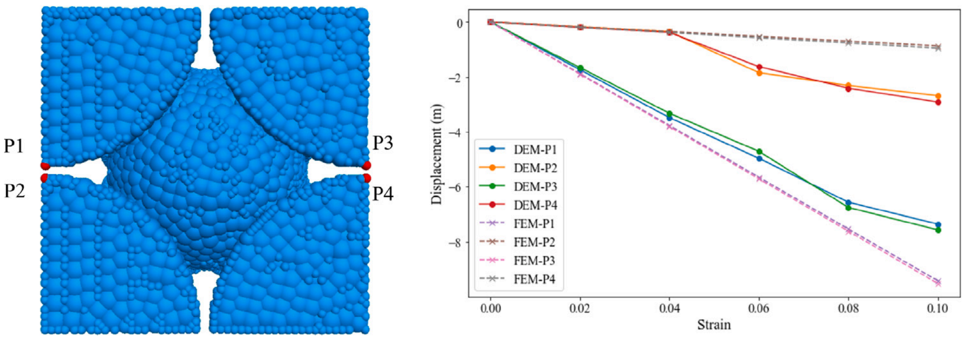

Fig. 20. The comparison of simulation results from DEM and FEM of the BCC model.

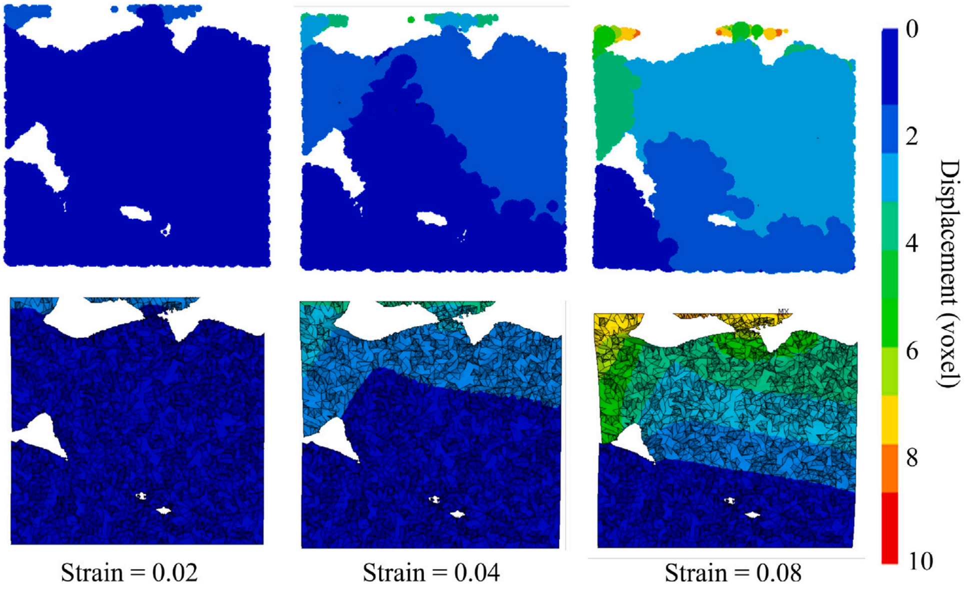

Fig. 21. The simulation of porous media by DEM and FEM. The top row is DEM results, and the bottom row is FEM results.

P4 remain almost unchanged. Upon reaching a strain of 0.04, contact occurs. Points P1 and P3 are resisted by points P2 and P3. Conversely, points P2 and P3 begin to move downward. The simulation results from FEM and DEM align well before contact, demonstrating the capability of DEM. The divergence between FEM and DEM after contact highlights DEM's proficiency in handling contact problems.

4.3. Porous media

The porous media model, denoted as Case 9 in Section 2, is taken from a digital rock sample of sandstone (Neumann et al., 2020). This model's geometry is notably complex. In our comparison, the DEM model is composed of a set of spheres, whereas the FEM model utilizes tetrahedrons. Achieving an identical cross-sectional geometry in both models is challenging; nevertheless, efforts are made to align the cross-sections as closely as possible. We present a cross-section illustrating the displacement along the z-axis under various strain levels.

As shown in Fig. 21, the results of the DEM and FEM simulations show slight differences, yet there is a high degree of correlation in the displacement distributions between the two numerical approaches. Notably, the triangular void on the left side becomes closed, and the smaller void at the lower right disappears. Upon reaching a strain of 0.1, the upper left section of the FEM model exhibits a slight twist due to penetration at the contact area. Fig. 22 illustrates the displacement comparison of four control points in a porous material model. These points are located at the corners of an inherited cubic, as shown in the left image of the figure. Their coordinates are $(75,75,75)$, $(25,75,75)$, $(75,25,25)$, and $(25,75,25)$. The DEM results align well with the FEM results overall, though some discrepancies arise when the strain exceeds 0.04. Additionally, due to the complex geometry of this sample, the displacements of P1 and P2 differ, even though they are at the same level (both at 75 along the z-axis).

4.4. Fracture simulation

One of the main advantages of the DEM over the FEM is the ability to simulate fracturing processes. To validate the capacity of the proposed CT-image-based DEM model for porous media for simulating the whole process of compression-induced fracture, the BCC model is used, as shown in Fig. 23. In this simulation, the microscopic mechanical parameters tensile strength and cohesion are reduced to 4e3 and 5e3, respectively, so the model would break under the given compression loading.

Fig. 23 shows the compression process of the BCC model, where the first image shows the stress–strain curve. Initially, with the increase of strain (till about 0.01), the stress increases linearly, showing the porous material is under elastic deformation. Then the pick strength appears when the strain reaches 0.012, and the pick strength is $50,000$Pa, after which the stress reduces with the strain. When the strain becomes greater than 0.02, notable fractures develop in the model. As the strain

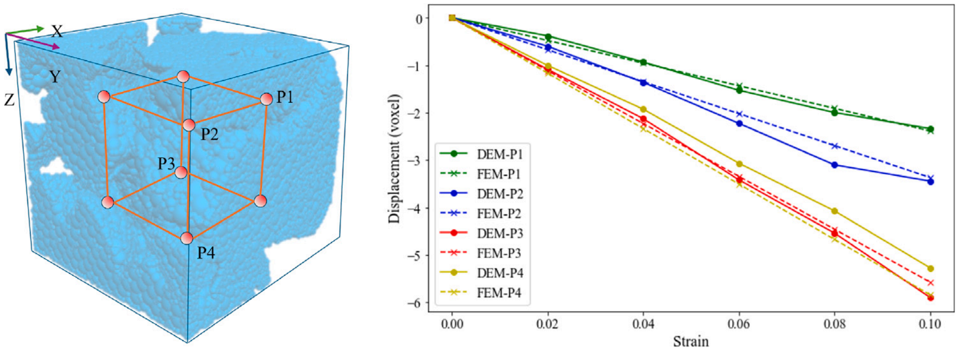

Fig. 22. The comparison of simulation results from DEM and FEM of a porous material model.

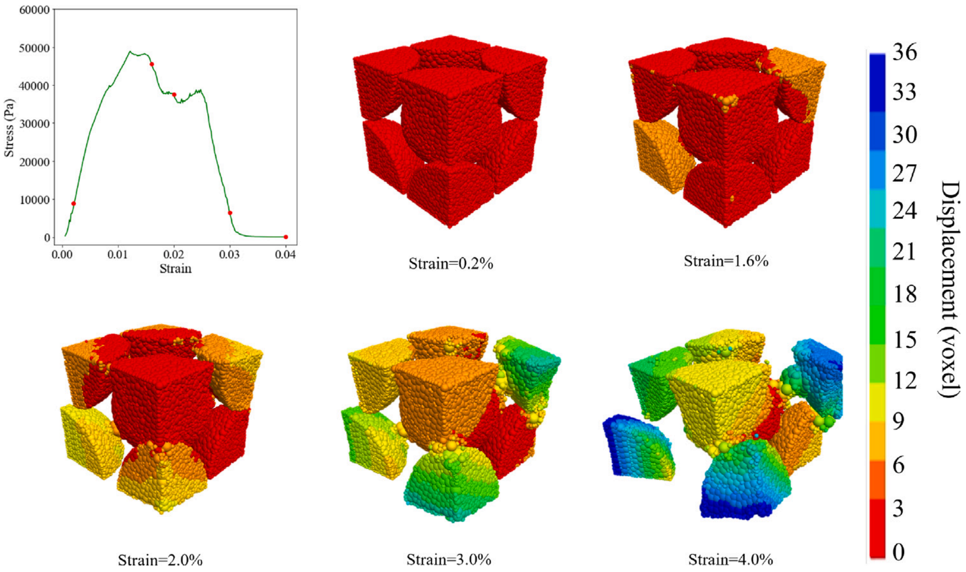

Fig. 23. The simulation of uniaxial compression of the BCC model. The first image shows the stress–strain curve, and the following five images of the BCC model correspond to the marked red points in the stress–strain curve.

reaches 0.04, the model breaks into several pieces, and the resistant stress reduces to 0.

5. Strain-sensitive properties of porous media

Sensitivity to stress and strain plays a crucial role in porous media, as the physical and geometric characteristics of these materials vary under different in-situ stress conditions. The proposed CT-image based DEM method can help to investigate how the properties of porous media respond to stress and deformation. Specifically, nine properties are studied in this work, including permeability and eight morphological descriptors. The eight descriptors can be classified into three groups (see Table 4): the Kozeny–Carman group includes tortuosity, porosity, specific surface area; the fractal group includes fractal dimension, lacunarity, succolarity; and the correlation function group include characteristic length I and characteristic length II.

To support this investigation, five sandstone digital rock models are sourced from the Digital Rocks Portal online library (Neumann et al., 2020). They come from the same resource as nine samples used in previous sections. Each model consists of $1000 \times 1000 \times 1000$ voxels and voxel dimensions of 2.25 μm. From these models, we randomly extract 400 subdomain samples, each measuring $200 \times 200 \times 200$ voxels, to form our digital rock database. Each subdomain sample is converted into a DEM model, from which a DEM simulation is performed to obtain six deformation states of uniaxial compression test, corresponding to nominal strains of 0.005, 0.010, 0.015, 0.020, 0.025 and 0.030. The parameters used in DEM simulation are the same as presented in Table 1. These six deformed states are then compared with the original undeformed state to evaluate permeability and various morphology properties.

Table 4
The list of eight morphological descriptors.

Groups	Descriptors	Representative reference
Fractal	Fractal dimension	Peng et al. (2011)
	Lacunarity	Allain and Cloitre (1991)
	Succolarity	De Melo and Conci (2008)
Kozeny–Carman	Tortuosity	Clennell (1997)
	Porosity	Carman (1997)
	Specific surface area	Detsi et al. (2011)
Correlation function	Characteristic length I	Coker et al. (1996)
	Characteristic length II	Coker et al. (1996)

5.1. Permeability under different strain of porous media

The permeability describes the ability of porous media to transport fluid. In the oil and gas industry, measuring the permeability of well-processed reservoir rock samples is a routine laboratory experiment. It is well-known that the in-situ stresses affect strongly the flow paths in porous media including pores, throats and fractures, which has a direct impact on the permeability measurement (Xu et al., 2018).

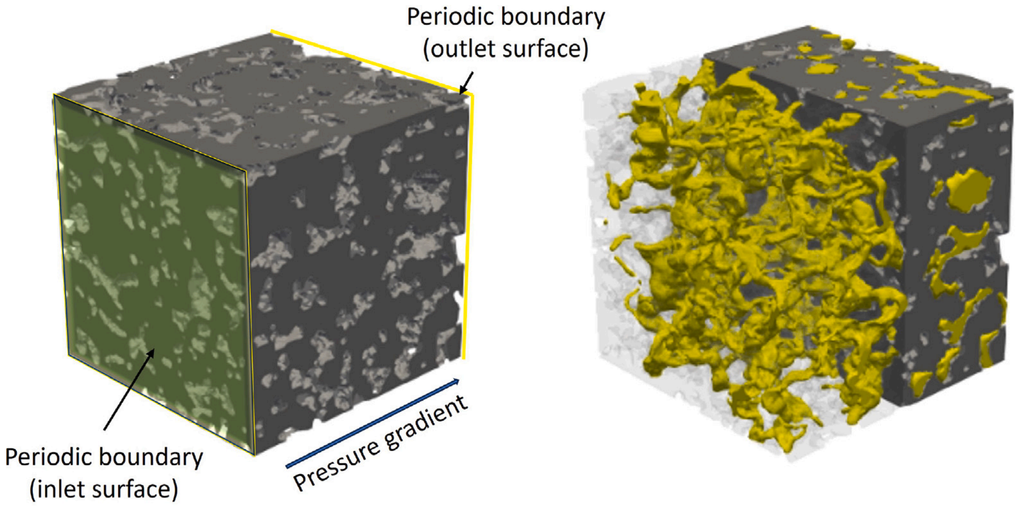

Fig. 24. An example of simulation for permeability.

In our study, the permeability is derived from Lattice Boltzmann Method (LBM) simulation of digital rock samples. To account for the effect of stress, the deformed DEM models are converted into 3D binary images. These images serve as the input for LBM simulations, with two surfaces perpendicular to the x-axis configured with periodic boundaries and the remaining four surfaces enclosed by bounce-back boundaries. A pressure gradient along the x-axis drives the fluid flow. Fig. 24 shows an example of LBM simulation for permeability. The direct result is a dimensionless value with the unit of voxel^2, while the physical value of permeability is obtained by applying a scaling factor (2.25 μm/voxel)^2.

The histogram in Fig. 25 illustrates the distribution of permeability values for the 400 undeformed digital rock samples. The permeability values are plotted along the x-axis, ranging from 0.05 to 0.30, with corresponding frequencies shown on the y-axis as percentages. The distribution is characterized by a prominent peak at lower permeability values, indicating a higher frequency of samples with lower permeability, around 0.05. The frequency gradually decreases as permeability increases, showing a skewed distribution towards lower values. This pattern suggests that the majority of the materials exhibit relatively low permeability, with fewer occurrences of materials having higher permeability.

In the second graph of Fig. 25, we present the normalized permeability (using the permeability of the undeformed digital rock sample as the normalization factor) as a function of strain, based on a comprehensive dataset comprising 400 simulation results. The mean normalized permeability, depicted by the solid black line, demonstrates a clear exponential-law decay with increasing strain, indicative of the material's response under stress. This trend is further bounded by the upper (red dashed line) and lower (blue dashed line) limits, which encapsulate the range of variability observed across the simulations. Initially, the decrease in permeability is quite steep, as shown by the near-vertical descent at lower strain values. However, as strain increases beyond approximately 0.015, the rate of decrease in permeability moderates, suggesting a diminishing sensitivity to further strain increments. This behaviour points to a potential threshold beyond which the material's structure may be less responsive to additional deformation, providing critical insight for applications involving stress management in porous media.

5.2. Eight descriptors under different strain levels of porous media

5.2.1. Porosity

Porosity is defined as the proportion of void or fluid spaces within the total volume of image voxels. As illustrated in the left histogram of Fig. 26, the porosity values of 400 undeformed digital rock samples range from 0.22 to 0.40, with the majority clustered between 0.225 and 0.300. This distribution suggests that the sandstone samples analysed in this study predominantly exhibit low porosity, which is typically associated with reduced permeability.

In the right graph of Fig. 26, the variation in porosity under different strain levels is depicted. Although the trends in porosity superficially mirror those observed in permeability, they more closely adhere to a biphasic linear relationship rather than a straightforward correlation. Initially, porosity sharply declines as strain increases from 0 to 0.005, followed by a more gradual, near-linear decrease as strain continues to rise. These patterns underscore a significant interdependence between porosity and permeability, highlighting how structural changes within the material influence its hydraulic properties.

5.2.2. Tortuosity

Tortuosity is simply defined as the ratio between the actual length of flow path and the straight-line distance through the medium in the direction of macroscopic flow. In this work, tortuosity is calculated as an inverse problem solution from the simulated flow field, as derived by Duda et al. (2011).

The histogram in Fig. 27 presents the distribution and evolving trends of tortuosity across the digital rock sample set. The tortuosity values range from 1.35 to 1.55, predominantly centred around 1.47. This central concentration implies that for a fluid particle traversing a straight-line distance of 100 voxels in the porous medium, the actual length of travel path would approximate 147 voxels. The graph in Fig. 27 shows the trend in tortuosity exhibits an inverse relationship with porosity changes. As strain increases from 0 to 0.005, the mean tortuosity sharply rises, followed by a more gradual increase with further strain application. Notably, tortuosity expands by approximately 2.5% when the porous media undergoes a compression of about 3%, underscoring the significant impact of structural deformations on the fluid pathways within the medium.

5.2.3. Specific surface area

The specific surface area is defined as the ratio of the interface area between solid and pore space to the bulk volume of the sample, and it provides insight into the texture of the pore network. The histogram in Fig. 28 displays the distribution and evolution of specific surface area within the 400 digital rock samples. The values of the specific surface area range from 0.16 to 0.24, exhibiting a more complex distribution pattern with multiple centres observed at 0.17, 0.19, 0.21, and 0.22. This irregularity suggests variations in pore complexity across different samples.

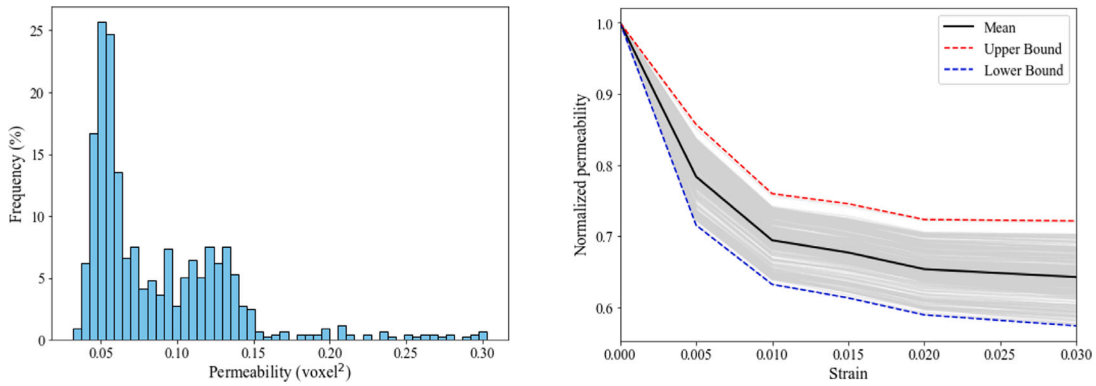

Fig. 25. The distribution and change trend of permeability.

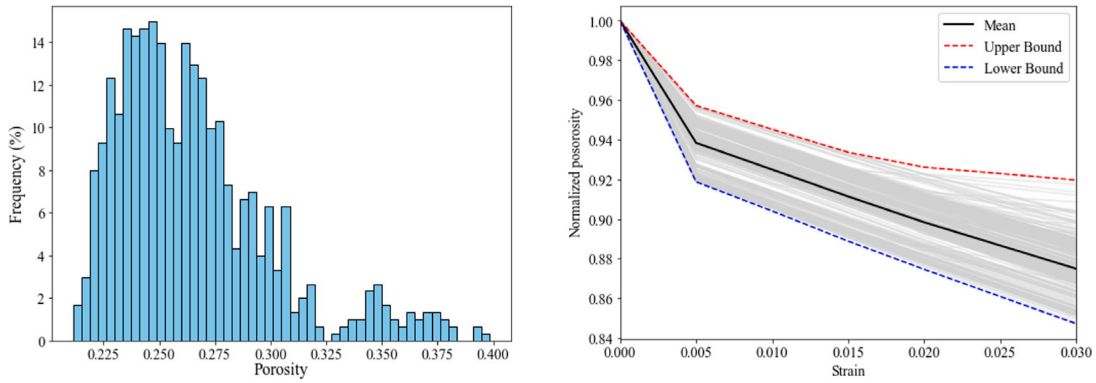

Fig. 26. The distribution and change trend of porosity.

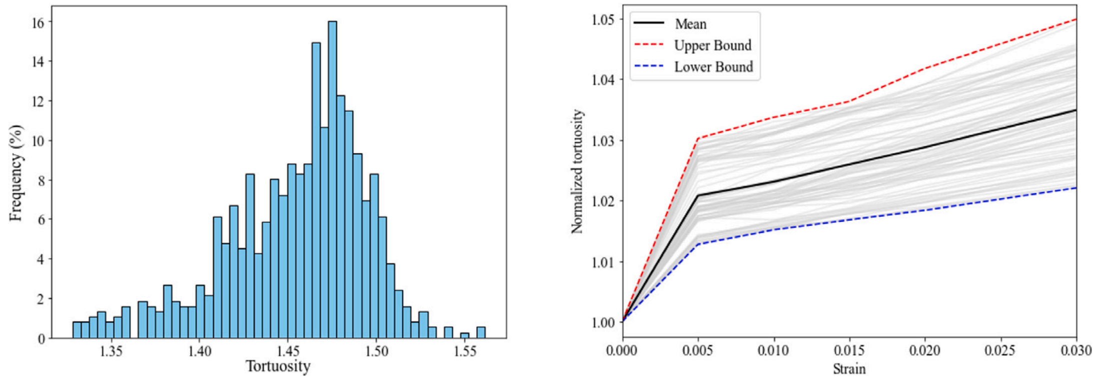

Fig. 27. The distribution and change trend of tortuosity.

Regarding the influence of stress and deformation, the specific surface area shows a marked increase as strain intensifies from 0 to 0.005, followed by a slower ascent until a strain of 0.01. Beyond this point, the specific surface area exhibits a linear decline with increasing strain. The peak mean value of the normalized specific surface area reaches approximately 1.05, indicating significant variations in pore surface exposure under stress conditions.

5.2.4. *Fractal dimension*

The fractal dimension represents how much an object occupies the metric space, and can be computationally calculated by the popular box-counting algorithm. The basic idea of the box-counting method is to count the number of boxes of a given size needed to cover the object or pattern, and then plot the logarithm of the box size against the logarithm of the number of boxes. The slope of the resulting line gives an estimate of the fractal dimension (Peng et al., 2011).

As shown in the histogram in Fig. 29, the distribution of fractal dimension is quite unique with all values highly concentrated at two centres, 2.878 and 2.887. There is a large gap between these two groups. Shown in the second graph in Fig. 29, the fractal dimension tends to converge with increasing strain in the porous media. Initially (at no compression strain), the fractal dimension spans from 2.876 to 2.888, with most samples' values narrowing to a range between 2.877 and 2.878. The mean fractal dimension decreases sharply from 2.882 to approximately 2.878 as the strain increases from 0 to 0.005, thereafter remaining nearly constant. The mean values tend to be closer to the upper limit of this range.

5.2.5. *Lacunarity*

Lacunarity quantifies the extent of spatial unevenness or the patchy nature observed in fractal patterns. This mathematical concept describes how gaps or voids are distributed across various scales or

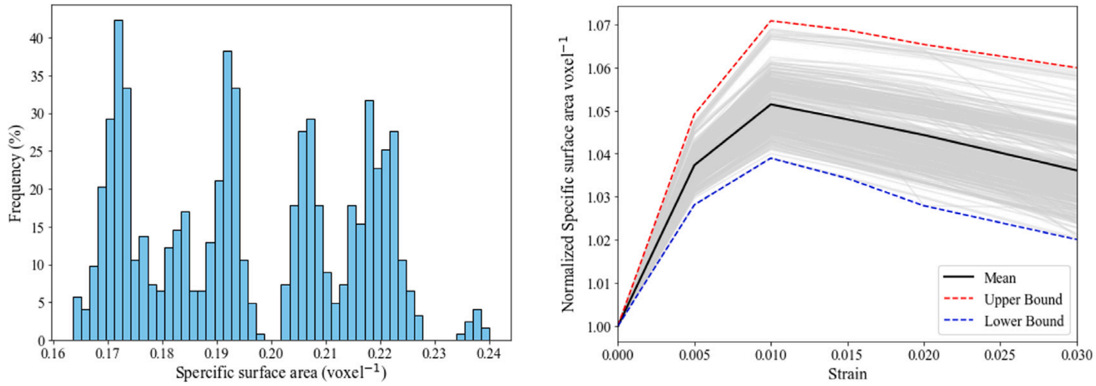

Fig. 28. The distribution and change trend of specific surface area.

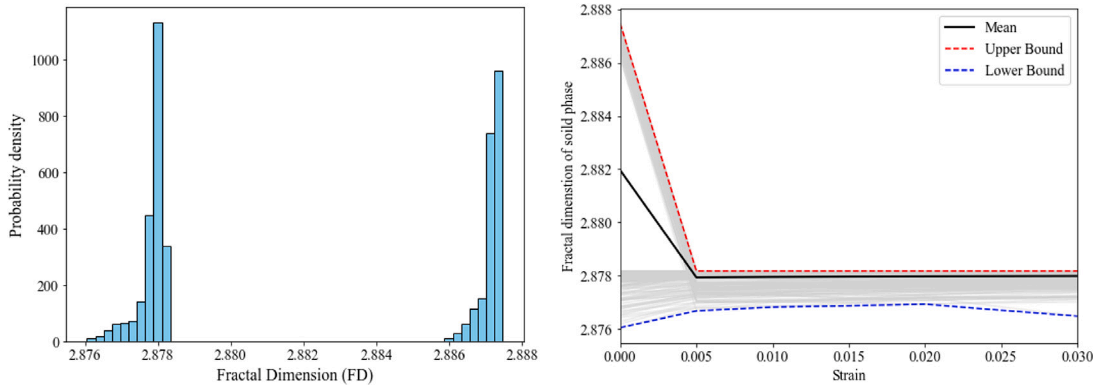

Fig. 29. The distribution and change trend of fractal dimension.

resolutions within a pattern. Through lacunarity analysis, one can measure the variety in pore sizes and shapes, and assess the connectivity and complexity of the pore structure. The calculation of lacunarity employs the box-counting method, indicating that the outcomes are influenced by the chosen box size for the analysis. In samples of porous media, it is observed that lacunarity values tend to decrease as the box size increases (Allain and Cloitre, 1991). This section discusses the lacunarity values obtained for a box size of 4 voxels.

The histogram in Fig. 30 illustrates the distribution and variation trends of lacunarity when the box size is set to 4 voxels. The lacunarity values spread between 0.52 and 0.65, and can be grouped into four categories centred around 0.53, 0.57, 0.60, and 0.64 respectively. The second graph in Fig. 30 shows the pattern of lacunarity changes with strain, for a box size of 4. A complex trend is observed: it initially decreases as strain increases, hitting a low at a strain of 0.01; from a strain of 0.010 to 0.020, the lacunarity values increase before dropping again, reaching another minimal point at a strain of 0.030.

5.2.6. Succolarity

Succolarity is also a key parameter in fractal theory. It presents the connectivity, tortuosity and percolation of porous material. It can measure the connectivity of a sample in different directions and distinguish different structures of the porous media that have the same fractal dimension and lacunarity. Compared with fractal dimension and lacunarity, succolarity is more appropriate for the permeability prediction of a sandstone reservoir (Falconer, 2004). The calculation method of succolarity was firstly mentioned by De Melo and Conci (2008). An ideal box-counting method was used in the calculation. de Melo and Conci (2013) showed that the change of box size had little influence on the value of succolarity. Here we present the succolarity with box size of 5.

Fig. 31 shows the distribution of succolarity at the initial undeformed condition and the change trend with strain. The initial values of succolarity range from 0.2 to 0.4, and the major part fall in the range of $0.2 - 0.325$, as an normal distribution. The change trend of succolarity shows a similar scheme as the change trend of porosity, a biphasic linear relationship. When the porous media is compressed of about 3%, the succolarity reduces about 15%.

5.2.7. Characteristic length

The two-point correlation function $S_2(\boldsymbol{r}_1, \boldsymbol{r}_2)$ explains the probability of finding two points both located in the pore space of binary image, and $\Delta r = \|\boldsymbol{r}_1 - \boldsymbol{r}_2\|$ is the distance between these two points. The two-point correlation function can be presented as the function of Δr:

$$S_2(\boldsymbol{r}_1, \boldsymbol{r}_2) = S_2(\Delta r) \tag{6}$$

The result of the two-point correlation function is an array of probabilities corresponding to varying distances. To facilitate integration into the neural network, specific scalar values representing the function's characteristics have been proposed (Coker et al., 1996):

$$l_{\mathrm{I}} = \int_0^{\infty} \left(S_2(\Delta r) - \phi^2\right) \mathrm{d}(\Delta r) \tag{7}$$

$$l_{\mathrm{II}} = \sqrt{\int_0^{\infty} \left(S_2(\Delta r) - \phi^2\right) \Delta r \ \mathrm{d}(\Delta r)} \tag{8}$$

where ϕ is the porosity of the samples, l_{I} the characteristic length I, and l_{II} the characteristic length II.

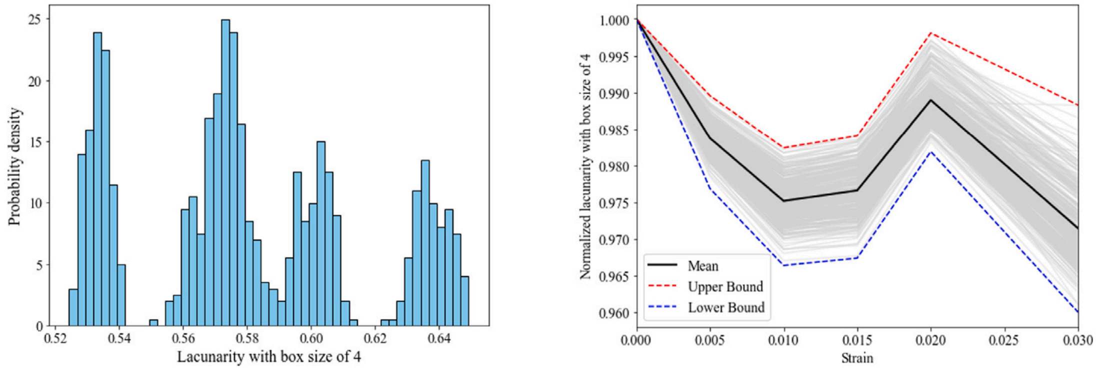

Fig. 30. The distribution and change trend of lacunarity.

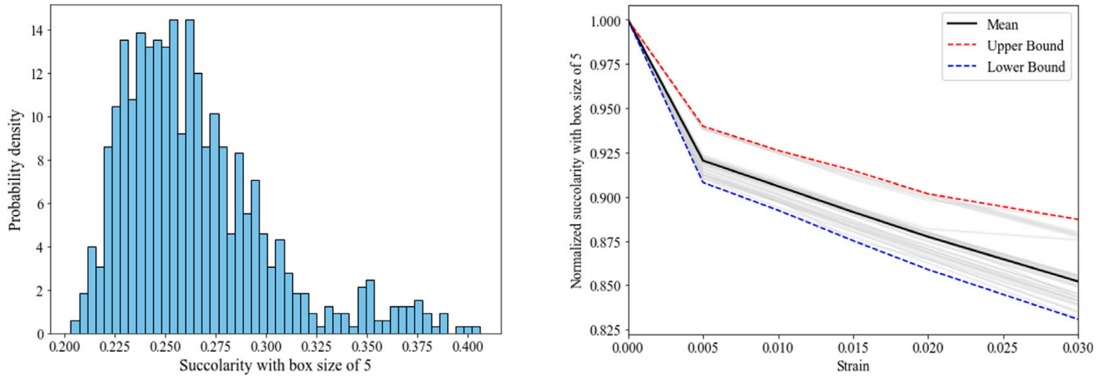

Fig. 31. The distribution and change trend of succolarity.

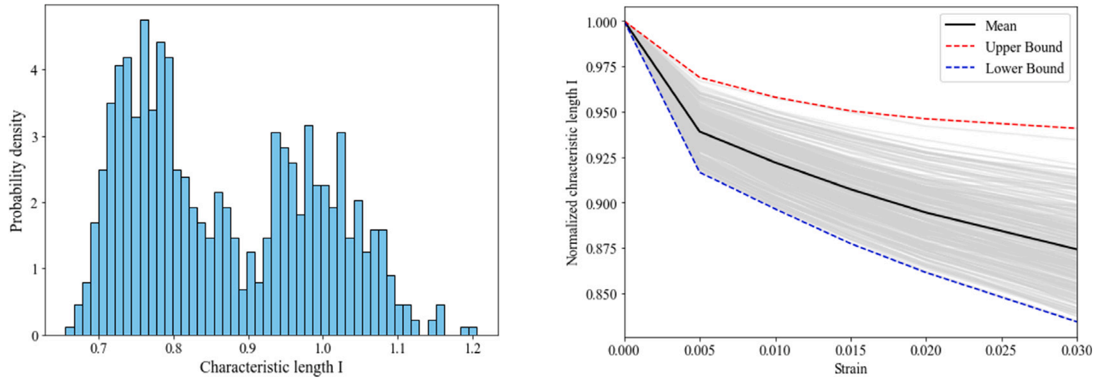

Fig. 32. The distribution and change trend of the characteristic length I.

Fig. 32 illustrates the initial distribution and the evolving pattern of the characteristic length I under strain. The characteristic length I varies between 0.7 and 1.2, forming two normally distributed groups centred at 0.78 and 1.0, respectively. Its evolution is characterized by a two-phase linear reduction. Initially, the average value of characteristic length I rapidly drops to approximately 0.93 at a strain of 0.005, followed by a gradual decrease to 87.5% of its original value.

Fig. 33 illustrates the initial distribution and the evolving pattern of the characteristic length II during deformation. The left histogram presents the distribution characterized by a modal peak and a right-skewed tail, indicating a prevalent central tendency with decreasing frequencies as the values escalate. The evolution of the characteristic length II mirrors this pattern. Initially, the average value of the normalized characteristic length II rapidly drops to 0.90 as the strain reaches 0.005, followed by a gradual decline to 0.80. Ultimately, the values of normalized characteristic length vary between 0.70 and 0.95 in the final state.

6. Conclusion

In this paper, we present a CT-image based DEM method to investigate the strain-sensitive properties of porous media. The proposed DEM models have two main advantages. The size distribution, extent of overlap, and total number of spheres used in the models can be explicitly controlled by three algorithmic parameters: the relaxing parameter

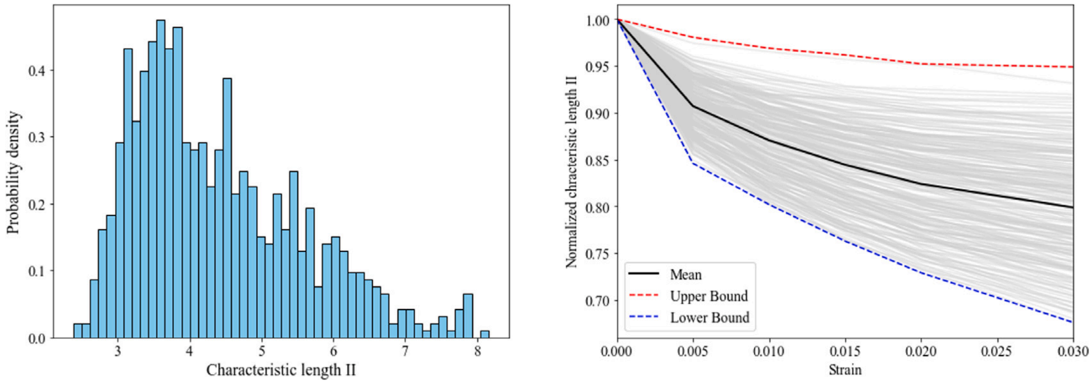

Fig. 33. The distribution and change trend of the characteristic length II.

ϵ, the maximum radius $R_{\max}$, and the minimum radius $R_{\min}$. Besides the flexible control, our proposed DEM models focus on the system-level morphology features of porous media, instead of the shapes of individual grains/particles.

Using nine cubic samples of porous materials, a range of simulation experiments are conducted to examine the performance of our DEM model construction. We also investigate the influence of the control parameters on the elastic mechanical properties by subjecting one of the cubic samples to uniaxial compressive loading. Our evaluation of the parameters' influence provides guidance for selecting the optimal parameter combinations, which must work in conjunction with micro-scale parameters to achieve the desired macro-scale mechanical properties. The proposed DEM models are compared with standard FEM simulation on a range of porous media structures, demonstrating good agreement in all cases.

The proposed method has been applied to examine the deformation sensitivity (stress sensitivity) of porous media. In this study, permeability and eight morphological descriptors are studied. The permeability decreases exponentially with the strain in porous media. As the strain increases, its influence diminishes. Among the eight descriptors, tortuosity increases with strain, while specific surface area initially increases and then decreases. The fractal dimension tends to converge towards a consistent value as strain progresses. Lacunarity exhibits a complex variation with strain. Porosity, succolarity, and characteristic lengths I and II exhibit similar trends, demonstrating a two-stage linear decline in response to increasing strain.

CRediT authorship contribution statement

Shan Zhong: Writing – original draft, Visualization, Validation, Methodology, Investigation. **Xiangyun Ge:** Writing – review & editing, Investigation. **Hywel R. Thomas:** Supervision. **Chenfeng Li:** Writing – review & editing, Supervision, Methodology, Funding acquisition, Conceptualization.

Declaration of competing interest

The authors declare that they have no known competing financial interests or personal relationships that could have appeared to influence the work reported in this paper.

Data availability

No data was used for the research described in the article.

Acknowledgements

The authors would like to thank the support from the China Scholarship Council, Swansea University, United Kingdom, and the Royal Society, United Kingdom (Ref.: IEC\NSFC\191628).

References

Al-Rifaie, A., Guan, Z., Jones, S., 2017. Quasi-static analysis of end plate beam-to-column connections. Int. J. Civ. Environ. Eng. 11 (7), 936–941.

Allain, C., Cloitre, M., 1991. Characterizing the lacunarity of random and deterministic fractal sets. Phys. Rev. A 44 (6), 3552–3558. http://dx.doi.org/10.1103/PhysRevA.44.3552, Retrieved from https://www.scopus.com/inward/record.uri?eid=2-s2.0-0001445940&doi=10.1103%2fPhysRevA.44.3552&partnerID=40&md5=9e27d83640c101a1a4aaef6cd9d30ffe.

Arand, F., Hesser, J., 2017. Accurate and efficient maximal ball algorithm for pore network extraction. Comput. Geosci. 101, 28–37.

Arns, C.H., Knackstedt, M.A., Pinczewski, W.V., Garboczi, E.J., 2002. Computation of linear elastic properties from microtomographic images: Methodology and agreement between theory and experiment. Geophysics 67 (5), 1396–1405.

Bakhshian, S., Sahimi, M., 2016. Computer simulation of the effect of deformation on the morphology and flow properties of porous media. Phys. Rev. E 94 (4), 042903. http://dx.doi.org/10.1103/PhysRevE.94.042903.

Capozza, R., Hanley, K., 2021. A hierarchical, spherical harmonic-based approach to simulate abradable, irregularly shaped particles in DEM. Powder Technol. 378, 528–537. http://dx.doi.org/10.1016/j.powtec.2020.10.015, Retrieved from https://www.sciencedirect.com/science/article/pii/S003259102030958X.

Carman, P., 1997. Fluid flow through granular beds. Chem. Eng. Res. Des. 75, S32–S48. http://dx.doi.org/10.1016/S0263-8762(97)80003-2, Retrieved from https://www.sciencedirect.com/science/article/pii/S0263876297800032.

Chai, H., Xie, Z., Feng, Z., Luo, S., Huang, J., 2021. Three-dimensional deformation dynamics of porous titanium under uniaxial compression. Mater. Charact. 182, 111494.

Clennell, M.B., 1997. Tortuosity: a guide through the maze. Geol. Soc. Lond. Spec. Publ. 122 (1), 299–344.

Coker, D.A., Torquato, S., Dunsmuir, J.H., 1996. Morphology and physical properties of Fontainebleau sandstone via a tomographic analysis. J. Geophys. Res.: Solid Earth 101 (B8), 17497–17506.

Cortés, C., Osorno, M., Uribe, D., Steeb, H., Ruiz-Salguero, O., Barandiarán, I., Flórez, J., 2019. Geometry simplification of open-cell porous materials for elastic deformation FEA. Eng. Comput. 35, 257–276.

Cundall, P.A., Strack, O.D., 1979. A discrete numerical model for granular assemblies. Geotechnique 29 (1), 47–65. http://dx.doi.org/10.1680/geot.1979.29.1.47, Retrieved from https://www.icevirtuallibrary.com/doi/abs/10.1680/geot.1979.29.1.47?casa_token=aZf5PA2GDZEAAAAA:fLBv26kIctXjZyW9oQdYKMRiguMTwHfbc7eyu7zt1UWw4aHuBvOdL06xiWiYdEaXNqFHbVYrXvRm.

De Melo, R., Conci, A., 2008. Succolarity: defining a method to calculate this fractal measure. In: 2008 15th International Conference on Systems, Signals and Image Processing. IEEE, pp. 291–294.

de Melo, R.H., Conci, A., 2013. How succolarity could be used as another fractal measure in image analysis. Telecommun. Syst. 52, 1643–1655.

Detsi, E., De Jong, E., Zinchenko, A., Vuković, Z., Vuković, I., Punzhin, S., Loos, K., Ten Brinke, G., De Raedt, H., Onck, P., et al., 2011. On the specific surface area of nanoporous materials. Acta Mater. 59 (20), 7488–7497.

Doroszko, M., Seweryn, A., 2020. Pore-scale numerical modelling of large deformation behaviour of sintered porous metals under compression using computed microtomography. Mech. Mater. 141, 103259.

Duan, K., Li, X., Kwok, C.-Y., Zhang, Q., Wang, L., 2021. Modeling the orientation- and stress-dependent permeability of anisotropic rock with particle-based discrete element method. Int. J. Rock Mech. Min. Sci. 147, 104884.

Duda, A., Koza, Z., Matyka, M., 2011. Hydraulic tortuosity in arbitrary porous media flow. Phys. Rev. E 84 (3), 036319.

Falconer, K., 2004. Fractal Geometry: Mathematical Foundations and Applications. John Wiley & Sons.

Ferellec, J.-F., McDowell, G., 2008. A simple method to create complex particle shapes for DEM. Geomech. Geoeng.: Int. J. 3 (3), 211–216. http://dx.doi.org/10.1080/17486020802253992, Retrieved from https://www.tandfonline.com/doi/abs/10.1080/17486020802253992.

Ferellec, J.-F., McDowell, G.R., 2010. A method to model realistic particle shape and inertia in DEM. Granul. Matter 12, 459–467. http://dx.doi.org/10.1007/s10035-010-0205-8, Retrieved from https://link.springer.com/article/10.1007/s10035-010-0205-8.

Fu, Y., Wang, L., Zhou, C., 2010. 3D clustering DEM simulation and non-invasive experimental verification of shear localisation in irregular particle assemblies. Int. J. Pavement Eng. 11 (5), 355–365.

Gans, H., Woodmansee, P., 1992. An improved method of modeling porous materials using finite elements. Comput. Struct. 44 (5), 1055–1063.

Gao, H., Zhang, D., Lu, J., Yin, G., Wu, M., 2020. Experimental study on influence of intermediate principal stress on the permeability of sandstone. Transp. Porous Media 135 (3), 753–778.

Ghosh, S., Lee, K., Raghavan, P., 2001. A multi-level computational model for multi-scale damage analysis in composite and porous materials. Int. J. Solids Struct. 38 (14), 2335–2385.

Hagenmuller, P., Chambon, G., Naaim, M., 2015. Microstructure-based modeling of snow mechanics: a discrete element approach. Cryosphere 9 (5), 1969–1982. http://dx.doi.org/10.5194/tc-9-1969-2015, Retrieved from https://tc.copernicus.org/articles/9/1969/2015.

Hössinger-Kalteis, A., Reiter, M., Jerabek, M., Major, Z., 2021. Overview and comparison of modelling methods for foams. J. Cell. Plast. 57 (6), 951–1001.

Hu, G., Zhou, B., Fu, R., Guo, Y., Han, C., Lv, K., 2021. Discrete element modeling of the compression molding of polymer–crystal composite particles. Powder Technol. 390, 112–125.

Huang, J., Xiao, F., Labra, C., Sun, J., Yin, X., 2021. DEM-LBM simulation of stress-dependent absolute and relative permeabilities in porous media. Chem. Eng. Sci. 239, 116633.

Iio, S., Hasegawa, K., Fushimi, S., Yonezu, A., Chen, X., 2016. On compressive deformation behavior of hollow-strut cellular materials. Mater. Des. 105, 1–8.

Kawamoto, R., Andò, E., Viggiani, G., Andrade, J.E., 2016. Level set discrete element method for three-dimensional computations with triaxial case study. J. Mech. Phys. Solids 91, 1–13. http://dx.doi.org/10.1016/j.jmps.2016.02.021, Retrieved from https://www.sciencedirect.com/science/article/pii/S002250961530154X.

Lai, Z., Zhao, S., Zhao, J., Huang, L., 2022. Signed distance field framework for unified DEM modeling of granular media with arbitrary particle shapes. Comput. Mech. 70 (4), 763–783.

Li, M., Yin, G., Xu, J., Cao, J., Song, Z., 2016. Permeability evolution of shale under anisotropic true triaxial stress conditions. Int. J. Coal Geol. 165, 142–148.

Lin, R., Ren, L., Zhao, J., Tan, X., Rasouli, V., Wang, X., Wu, J., Song, Y., Shen, C., 2022. Stress and pressure dependent permeability of shale rock: Discrete element method (DEM) simulation on digital core. J. Pet. Sci. Eng. 208, 109797. http://dx.doi.org/10.1016/j.petrol.2021.109797, Retrieved from https://www.sciencedirect.com/science/article/pii/S0920410521014170.

Lu, M., McDowell, G., 2007. The importance of modelling ballast particle shape in the discrete element method. Granul. Matter 9, 69–80. http://dx.doi.org/10.1007/s10035-006-0021-3, Retrieved from https://link.springer.com/article/10.1007/s10035-006-0021-3.

Luo, R., Chen, P., Yang, T., Zhang, H.Z., Li, P., Zeng, Y.W., 2011. The three-dimensional DEM modeling of gravel materials. In: Advanced Materials Research. Vol. 301, Trans Tech Publ, pp. 488–493.

Matsushima, T., Katagiri, J., Uesugi, K., Tsuchiyama, A., Nakano, T., 2009. 3D shape characterization and image-based DEM simulation of the lunar soil simulant FJS-1. J. Aerosp. Eng. 22 (1), 15–23.

Matsushima, T., Saomoto, H., 2002. Discrete element modeling for irregularly-shaped sand grains. In: NUMGE 2002. 5th European Conference Numerical Methods in Geotechnical Engineering. pp. 239–246.

Mede, T., Chambon, G., Hagenmuller, P., Nicot, F., 2018. A medial axis based method for irregular grain shape representation in DEM simulations. Granul. Matter 20 (1), 1–11.

Moës, N., Cloirec, M., Cartraud, P., Remacle, J.-F., 2003. A computational approach to handle complex microstructure geometries. Comput. Methods Appl. Mech. Engrg. 192 (28–30), 3163–3177.

Neumann, R., Andreeta, M., Lucas-Oliveira, E., 2020. 11 Sandstones: Raw, Filtered and Segmented Data. Digital Rocks Portal, http://dx.doi.org/10.17612/f4h1-w124, https://www.digitalrocksportal.org/projects/317.

Peng, R., Yang, Y., Ju, Y., Mao, L., Yang, Y., 2011. Computation of fractal dimension of rock pores based on gray CT images. Chin. Sci. Bull. 56, 3346–3357.

Potyondy, D., Cundall, P., 2004. A bonded-particle model for rock. Int. J. Rock Mech. Min. Sci. 41 (8), 1329–1364. http://dx.doi.org/10.1016/j.ijrmms.2004.09.011, Retrieved from https://www.sciencedirect.com/science/article/pii/S1365160904002874. (Rock Mechanics Results from the Underground Research Laboratory, Canada).

Roberts, A.P., Garboczi, E.J., 2000. Elastic properties of model porous ceramics. J. Am. Ceram. Soc. 83 (12), 3041–3048.

Roubin, E., Vallade, A., Benkemoun, N., Colliat, J.-B., 2015. Multi-scale failure of heterogeneous materials: A double kinematics enhancement for Embedded Finite Element Method. Int. J. Solids Struct. 52, 180–196.

Samaei, A., Chaudhuri, S., 2021. Mechanical performance of zirconia-silica bi-layer coating on aluminum alloys with varying porosities: Deep learning and microstructure-based FEM. Mater. Des. 207, 109860.

Silin, D., Patzek, T., 2006. Pore space morphology analysis using maximal inscribed spheres. Phys. A 371 (2), 336–360.

Stamati, O., Roubin, E., Andò, E., Malecot, Y., 2019. Tensile failure of micro-concrete: from mechanical tests to FE meso-model with the help of X-ray tomography. Meccanica 54 (4), 707–722. http://dx.doi.org/10.1007/s11012-018-0917-0.

Sun, W., Kuhn, M.R., Rudnicki, J.W., 2013. A multiscale DEM-LBM analysis on permeability evolutions inside a dilatant shear band. Acta Geotech. 8, 465–480. http://dx.doi.org/10.1007/s11440-013-0210-2.

Taghavi, R., 2011. Automatic clump generation based on mid-surface. In: Proceedings, 2nd International FLAC/DEM Symposium, Melbourne. pp. 791–797.

Tahmasebi, P., 2018. Packing of discrete and irregular particles. Comput. Geotech. 100, 52–61. http://dx.doi.org/10.1016/j.compgeo.2018.03.011, Retrieved from https://www.sciencedirect.com/science/article/pii/S0266352X18300855.

van Rietbergen, B., Weinans, H., Huiskes, R., Odgaard, A., 1995. A new method to determine trabecular bone elastic properties and loading using micromechanical finite-element models. J. Biomech. 28 (1), 69–81.

Wang, P., Gao, N., Ji, K., Stewart, L., Arson, C., 2020. DEM analysis on the role of aggregates on concrete strength. Comput. Geotech. 119, 103290.

Wang, G., Jiang, C., Shen, J., Han, D., Qin, X., 2019. Deformation and water transport behaviors study of heterogenous coal using CT-based 3D simulation. Int. J. Coal Geol. 211, 103204.

Wang, L., Park, J.-Y., Fu, Y., 2007. Representation of real particles for DEM simulation using X-ray tomography. Constr. Build. Mater. 21 (2), 338–346. http://dx.doi.org/10.1016/j.conbuildmat.2005.08.013, Retrieved from https://www.sciencedirect.com/science/article/pii/S0950061805002576.

Xu, C., Lin, C., Kang, Y., You, L., 2018. An experimental study on porosity and permeability stress-sensitive behavior of sandstone under hydrostatic compression: characteristics, mechanisms and controlling factors. Rock Mech. Rock Eng. 51, 2321–2338. http://dx.doi.org/10.1007/s00603-018-1481-6.

Yin, G., Li, M., Wang, J., Xu, J., Li, W., 2015. Mechanical behavior and permeability evolution of gas infiltrated coals during protective layer mining. Int. J. Rock Mech. Min. Sci. 80, 292–301.

You, Z., Adhikari, S., Emin Kutay, M., 2009. Dynamic modulus simulation of the asphalt concrete using the X-ray computed tomography images. Mater. Struct. 42 (5), 617–630.

Zhang, N., Hedayat, A., Han, S., Yang, R., Sosa, H.G.B., Cárdenas, J.J.G., Álvarez, G.E.S., 2021. Isotropic compression behavior of granular assembly with non-spherical particles by X-ray micro-computed tomography and discrete element modeling. J. Rock Mech. Geotech. Eng. 13 (5), 972–984.